Cell Reports

Article

Glucose metabolism and pyruvate carboxylase enhance glutathione synthesis and restrict oxidative stress in pancreatic islets

Graphical abstract

Highlights

- Glucose contributes to *de novo* glutathione (GSH) synthesis in pancreatic islets
- GSH synthesis is required for glucose-dependent restriction of ROS in inflammation
- Pyruvate carboxylase connects glucose to GSH synthesis

Authors

Accalia Fu, Lara van Rooyen, Lindsay Evans, ..., Loren D. Walensky, A.M. James Shapiro, Nika N. Danial

Correspondence

nika_danial@dfci.harvard.edu

In brief

Fu et al. identify a pyruvate carboxylase (PC)-dependent mode of enhancing GSH biosynthesis via augmented glucose metabolism. The PC-GSH antioxidant axis protects pancreatic islets from diabetes-associated inflammation and oxidative stress.

Fu et al., 2021, Cell Reports *37*, 110037
November 23, 2021
https://doi.org/10.1016/j.celrep.2021.110037

CellPress

Cell Reports

CellPress
OPEN ACCESS

Article

Glucose metabolism and pyruvate carboxylase enhance glutathione synthesis and restrict oxidative stress in pancreatic islets

Accalia Fu,[1,2] Lara van Rooyen,[1] Lindsay Evans,[1] Nina Armstrong,[1] Daina Avizonis,[3] Tatsuya Kin,[4] Gregory H. Bird,[5,6] Anita Reddy,[1,2] Edward T. Chouchani,[1,2] Marc Liesa-Roig,[7,8,9] Loren D. Walensky,[5,6] A.M. James Shapiro,[4] and Nika N. Danial[1,10,11,12,*]

[1]Department of Cancer Biology, Dana-Farber Cancer Institute, 450 Brookline Ave., Boston, MA 02115, USA
[2]Department of Cell Biology, Harvard Medical School, 240 Longwood Ave., Boston, MA 02115, USA
[3]Rosalind and Morris Goodman Cancer Institute, Metabolomics Innovation Resource, 1160 Pine Avenue, Montreal, QC H3A 1A3, Canada
[4]Clinical Islet Transplant Program, Department of Surgery, 2000 College Plaza, University of Alberta, Edmonton, AB T6G 2C8, Canada
[5]Department of Pediatric Oncology, Dana-Farber Cancer Institute, Boston, MA 02115, USA
[6]Linde Program in Cancer Chemical Biology, Dana-Farber Cancer Institute, Boston, MA 02115, USA
[7]Department of Medicine, Endocrinology, David Geffen School of Medicine at UCLA, 650 Charles E. Young Dr., Los Angeles, CA 90095, USA
[8]Department of Molecular and Medical Pharmacology, David Geffen School of Medicine at UCLA, 650 Charles E. Young Dr., Los Angeles, CA 90095, USA
[9]Molecular Biology Institute, UCLA, 614 Charles E. Young Dr., Los Angeles, CA 90095, USA
[10]Department of Medical Oncology, Dana-Farber Cancer Institute, Boston 02115, MA, USA
[11]Department of Medicine, Harvard Medical School, 240 Longwood Ave., Boston, MA 02115, USA
[12]Lead contact
*Correspondence: nika_danial@dfci.harvard.edu
https://doi.org/10.1016/j.celrep.2021.110037

SUMMARY

Glucose metabolism modulates the islet β cell responses to diabetogenic stress, including inflammation. Here, we probed the metabolic mechanisms that underlie the protective effect of glucose in inflammation by interrogating the metabolite profiles of primary islets from human donors and identified *de novo* glutathione synthesis as a prominent glucose-driven pro-survival pathway. We find that pyruvate carboxylase is required for glutathione synthesis in islets and promotes their antioxidant capacity to counter inflammation and nitrosative stress. Loss- and gain-of-function studies indicate that pyruvate carboxylase is necessary and sufficient to mediate the metabolic input from glucose into glutathione synthesis and the oxidative stress response. Altered redox metabolism and cellular capacity to replenish glutathione pools are relevant in multiple pathologies beyond obesity and diabetes. Our findings reveal a direct interplay between glucose metabolism and glutathione biosynthesis via pyruvate carboxylase. This metabolic axis may also have implications in other settings where sustaining glutathione is essential.

INTRODUCTION

Glucose metabolism is central to the function, proliferation, survival, and differentiation of β cells, indicating that the molecular effectors of glucose signaling in these cells control pathways beyond insulin secretion (Dadon et al., 2012; Fu et al., 2020; Levitt et al., 2011; Metukuri et al., 2012; Prentki et al., 2013). However, the spectrum and mechanisms underlying glucose regulation of β cell pathways are complex and remain incompletely defined, especially in the context of diabetes-related stress such as inflammation. This complexity is further reflected by the protective versus toxic outcomes of a physiological versus supraphysiological rise in glucose flux, respectively (Bensellam et al., 2012; Brereton et al., 2016; Lytrivi et al., 2020; Swisa et al., 2017). These outcomes are partly determined by the specific fate of metabolites downstream of glucose. Within this context, we have recently identified an anti-inflammatory role for anaplerotic entry of glucose-derived pyruvate into the tricarboxylic acid (TCA) cycle via pyruvate carboxylase (PC) (Fu et al., 2020). Specifically, PC activity augments the availability of aspartate for the aspartate-argininosuccinate shunt and activation of the urea cycle, thereby limiting arginine for nitric oxide (NO) synthesis and protecting β cells from inflammation toxicity (Fu et al., 2020).

The protective PC-urea cycle axis is activated upon physiologic increases in glucose metabolism, for example, through activation of glucokinase (GK; the hexokinase isoform in β cells) near its active site at a region engaged by the phosphorylated BCL-2 homology 3 (BH3) α helix of the BCL-2-associated agonist of cell death (BAD) protein (Fu et al., 2020; Ljubicic et al., 2015; Szlyk et al., 2014). This mode of GK activation conserves the enzyme's native K_M for glucose (Szlyk et al., 2014). In comparison, the PC-urea cycle axis is not activated in the

context of supraphysiologic increases in glucose metabolism as in chronic exposure to high glucose or naturally occurring GK gain-of-function mutations at the allosteric site, which drastically increase the enzyme's affinity for glucose (Fu et al., 2020). As such, genetic or chemical biology tools that activate GK by mimicking BAD phosphorylation, such as a BAD BH3 phosphomimic variant or hydrocarbon-stapled peptides containing a serine to aspartic acid substitution modeled after the phospho-BAD BH3 helix (BAD $SAHB_A$ SD), have proven useful for the discovery of fundamental metabolic mechanisms linking glucose to the outcomes of inflammation in β cells (Fu et al., 2020). Indeed, our recent application of these tools in conjunction with untargeted metabolomics analyses has uncovered several metabolic signatures associated with glucose-dependent protection of human donor islets from pro-inflammatory cytokines. One such protective signature is arginine metabolism, and its further characterization led to the discovery of glucose-dependent urea cycle activation (Fu et al., 2020). Additional metabolic signatures discovered from these and subsequent metabolomics analyses await secondary validation and functional interrogation. These additional pathways may work cooperatively with glucose modulation of arginine metabolism to shield β cells from inflammation.

Inflammation combined with extensive production of reactive oxygen species (ROS) and oxidative damage contributes to β cell decline in the diabetic milieu (Donath et al., 2013; Eizirik et al., 2009; Padgett et al., 2013; Gerber and Rutter, 2017; Newsholme et al., 2019; Prentice et al., 2014). Among antioxidant pathways, β cells rely more heavily on glutathione (GSH), glutaredoxin, and thioredoxin systems and have lower superoxide dismutase (SOD) and catalase activity (Miki et al., 2018; Petry et al., 2017; Stancill et al., 2019; Shalev, 2014). However, the potential for biosynthetic input into these antioxidant pathways is not fully known. The current study was motivated by unbiased discovery of metabolite profiles corresponding to *de novo* GSH synthesis and recycling in human donor islets under conditions where increased glucose metabolism protects from inflammation. Isotopic tracer studies coupled with functional interrogation of GSH metabolism revealed metabolic input from glucose into *de novo* GSH synthesis via PC attenuates the effect of pro-inflammatory cytokines and nitrosative stress in human and mouse islets. Our studies highlight a broader role for PC in β cell redox metabolism and the GSH system beyond its well-recognized effects on nicotinamide adenine dinucleotide phosphate (NADPH/$NADP^+$) ratios.

RESULTS

Metabolomic profiling reveals increased antioxidant potential and glucose contributions to GSH synthesis by phospho-BAD mimicry in human islets undergoing inflammation stress

To probe the broad spectrum of metabolic mechanisms whereby glucose protects β cells from inflammation stress, we examined pathways that are modulated by phospho-BAD mimicry in human donor islets treated with pro-inflammatory cytokines and subjected to untargeted metabolomics analysis (Fu et al., 2020). These comparisons were carried out after 24 h of cytokine treatment, a time point before significant cell death is detected. Pathway enrichment and topology analyses comparing islets treated with vehicle control (veh) or BAD $SAHB_A$ SD in the presence of pro-inflammatory cytokines (combination of interleukin-1β [IL-1β], tumor necrosis factor alpha [TNF-α], and interferon γ [IFNγ]) indicated significant impact of phospho-BAD mimicry on pathways related to GSH metabolism and reductive potential (Figure S1A). This dataset was next complemented with an independent targeted liquid chromatography-tandem mass spectrometry (LC-MS/MS) metabolomics analysis using additional human donor islets and showed phospho-BAD mimicry significantly elevates GSH, cystathionine, and cysteinylglycine levels in islets undergoing inflammation stress, predicting increased GSH synthesis and recycling (Figure 1; Tables S1 and S2). It is important to note that these steady-state metabolite levels reflect the net balance of several multifariously connected pathways as well as metabolite exchange with media. For this reason, they were predominantly used to obtain an initial overview without making definitive inferences about individual metabolic reactions. Within these data, we also considered the amino acid precursors for GSH, namely glutamate, cysteine, and glycine. Steady-state levels of glutamate were significantly higher in response to phospho-BAD mimicry (Figure 1; Table S1). Cysteine levels per se were not altered under these conditions, but precursor metabolite cystathionine and downstream metabolites taurine and hypotaurine were significantly elevated (Figure 1; Table S1), perhaps reflecting an overall increase in cysteine metabolism. In comparison, glycine and serine were significantly reduced under these conditions, perhaps due to their usage for cystathionine production; however, alternative explanations cannot be ruled out (Figure 1; Table S1). Interestingly, phosphoserine, which can replenish serine pools available for glycine and GSH synthesis (Yang and Vousden, 2016), was significantly higher (Figure 1; Table S1). Because phosphoserine is derived from the glycolytic intermediate 3-phosphoglycerate, its increase is consistent with published evidence that phospho-BAD mimicry enhances glycolysis through GK activation (Danial et al., 2008; Ljubicic et al., 2015; Szlyk et al., 2014) and increases in glycolytic metabolites in BAD $SAHB_A$ SD-treated β cells exposed to inflammatory cytokines (Figure S1B).

Based on the overall metabolite patterns mentioned above, we next undertook metabolic tracing studies to test the prediction that GSH biosynthesis is enhanced under conditions where increased glucose metabolism is protective, such as phospho-BAD mimicry. Specifically, we quantified the contribution of glucose-derived carbons to GSH pools in human islets treated with a uniformly labeled glucose tracer, [$^{13}C_6$]-glucose, under the same experimental setting as in Figure 1. These analyses showed that glucose carbons can normally label ~25% of the total GSH pool in human islets (Figure 2A, [^{13}C]-GSH in PBS vehicle control treatment). Such robust incorporation of glucose carbons in GSH pools is in and of itself remarkable given that GSH synthesis is multiple steps removed from glucose-derived metabolites in glycolysis and TCA cycle and that label dilution through mixing of metabolite pools can mask the true contributions from glucose. Phospho-BAD mimicry increases ^{13}C incorporation from glucose into GSH in response to cytokine treatment (Figures 2A and 2B; [^{13}C]-GSH in BAD $SAHB_A$ SD

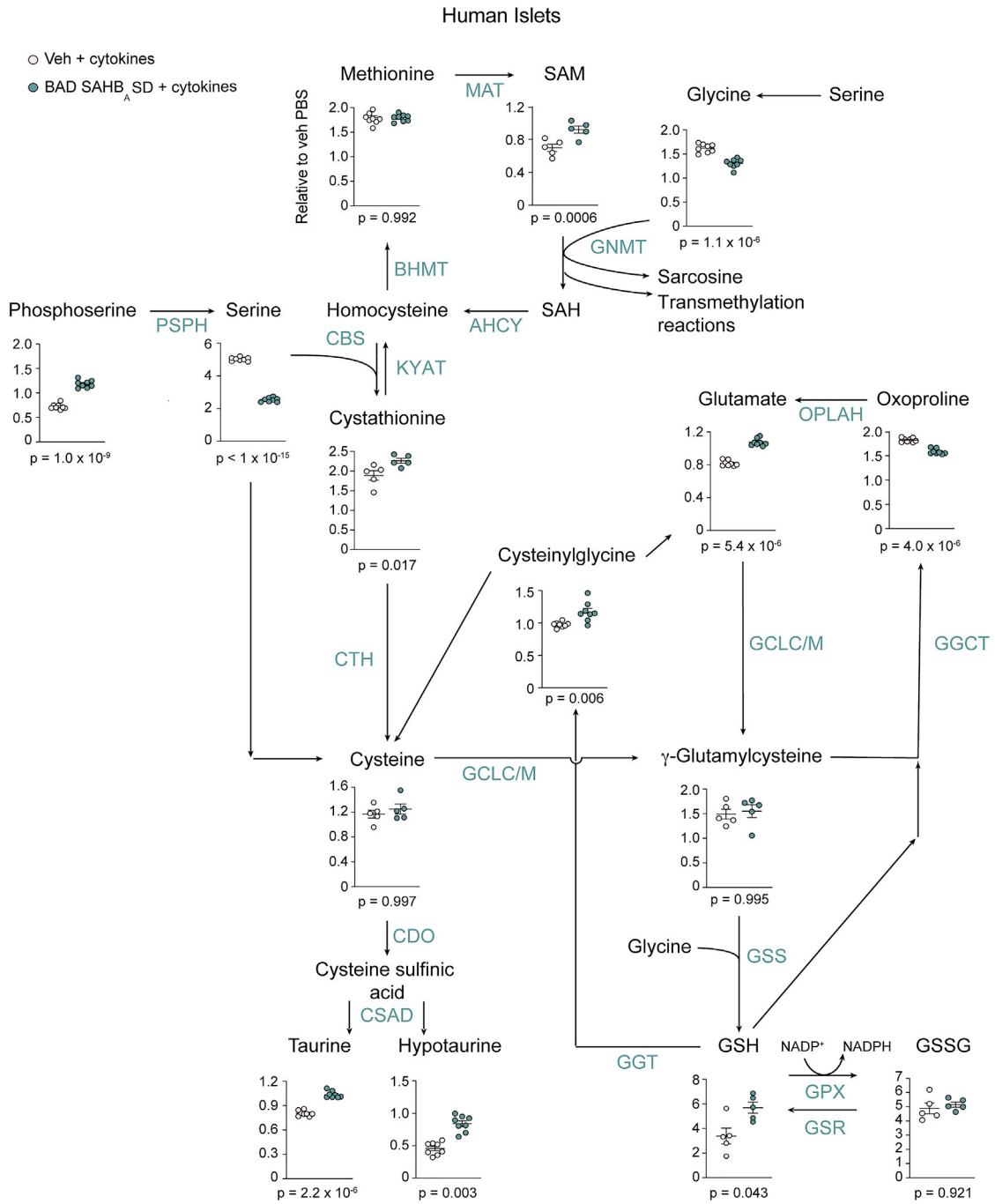

Figure 1. Metabolic profiling predicts increased antioxidant potential by phospho-BAD mimicry in human islets undergoing inflammation stress

Quantification of metabolites related to glutathione (GSH) metabolism, including synthesis (methionine, cysteine, serine, glycine, and glutamate) and recycling (oxoproline and cysteinylglycine) pathways in human islets cultured in Prodo Islet Media (Standard) (PIM(S)) media containing 5.8 mM glucose and treated for 24 h with inflammatory cytokines (10 ng/mL TNF-α, 10 ng/mL IL-1β, and 100 ng/mL IFNγ). Values are shown relative to vehicle control (veh) PBS set to 1. All metabolites except GSH, cystathionine, cysteine, γ-glutamylcysteine, and S-adenosylmethionine (SAM) were measured by untargeted metabolomics using human islets from n = 5 donors pooled and split into 8 replicates. For targeted measurement of GSH, cystathionine, cysteine, γ-glutamylcysteine, and SAM, islets from n = 5 donors were used.

Single arrows denote direct reactions; two arrows indicate multi-step reactions.

Abbreviations are as follows: AHCY, adenosylhomocysteinase; BHMT, betaine-homocysteine S-methyltransferase; CBS, cystathionine beta-synthase; CDO, cysteine dioxygenase type 1; CSAD, cysteine sulfinic acid decarboxylase; CTH, cystathionine gamma-lyase; GCLC/M, glutamate-cysteine ligase; GGCT,

(legend continued on next page)

versus vehicle cytokine treatment). BAD $SAHB_A$ SD-dependent increases in labeled GSH were concomitant with a reduction in the unlabeled pool of GSH, [^{12}C]-GSH, as expected (Figure 2A). Increased glucose contribution to GSH synthesis in this setting requires the GK-activating capacity of phospho-BAD mimicry because this increase was not observed in the presence of a stapled peptide modeled after a non-GK-activating BAD mutant harboring a triple alanine mutation in the BH3 domain (BAD $SAHB_A$ AAA) (Figures 2A and 2B) (Danial et al., 2008; Fu et al., 2020; Ljubicic et al., 2015). Of note, the expression of key enzymes involved in GSH metabolism (GSS, GCL, GSR, GPx1, and GPx4) was not altered in islets subjected to phospho-BAD mimicry (data not shown).

To gain more information about the routing of glucose carbons into GSH, we also calculated fractional labeling of different GSH isotopologs from [$^{13}C_6$]-glucose. Among GSH isotopologs with incorporation of at least one labeled carbon (M+1 through M+10), the abundance of M+2 (GSH labeled on two carbons) was most prominent (Figures 2C and 2D). Because MS does not provide positional information on the exact carbons that are labeled (unlike NMR), the precise origin of the M+2 GSH cannot be definitively inferred from these data, but possible synthesis routes to this isotopolog are described under discussion. Taken together, the above-mentioned combinations of untargeted, targeted, and tracer metabolomics in human islets identify GSH biosynthesis as an anabolic route for glucose carbons that is supported by phospho-BAD mimicry.

The BAD-GK axis restrains inflammation-induced ROS accumulation by supporting GSH synthesis

The above-mentioned observations suggest increased antioxidant capacity in response to phospho-BAD mimicry. This is also consistent with significantly higher ratios of GSH/oxidized GSH (GSSG), cysteine/cystine, and pyruvate/malate redox couples (Figure 3A). Notably, the level of GSSG is unaffected by phospho-BAD mimicry (Figure 1), indicating that the increase in the GSH/GSSG ratio is largely derived from higher levels of reduced GSH.

To provide independent corroborative evidence for the effect of phospho-BAD mimicry on GSH redox status, we undertook live imaging studies in human islets expressing glutaredoxin 1 fused to redox sensitive GFP2 (Grx1-roGFP2), which is an established biosensor for measuring the ratio of oxidized-to-reduced GSH (GSSG/GSH) in live cells (Morgan et al., 2011; Gutscher et al., 2008, 2009). This sensor was additionally engineered to selectively localize in the cytosol or the mitochondrial matrix, allowing quantification of GSSG/GSH ratios in these two separate subcellular compartments (Morgan et al., 2011; Roma and Jonas, 2020; Shum et al., 2021). An increase in the GSSG/GSH ratio was detected in the cytosol and the mitochondrial matrix upon cytokine exposure of vehicle-treated samples as expected, which was prevented by BAD $SAHB_A$ SD treatment (Figures 3B and S2A). Assessment of H_2O_2 levels using the Orp1 sensor also indicated that cytokine treatment led to increased cytosolic H_2O_2 levels, which was prevented by phospho-BAD mimicry (Figure 3C). Mitochondrial H_2O_2 levels were, however, unaffected by cytokines or phospho-BAD mimicry (Figure S2B), likely reflecting sufficient antioxidant effect from mitochondrial GSH in this setting.

As an independent readout of changes in antioxidant capacity, we next assessed total cellular ROS levels and found phospho-BAD mimicry blocked the rise in total ROS levels in human and mouse islets undergoing inflammation stress. This was evident from both pharmacological and genetic approaches to phospho-BAD mimicry using the BAD $SAHB_A$ SD stapled peptide (Figures 4A and 4B) as well as viruses bearing the corresponding full-length BAD BH3 phospho-mimic mutant (BAD SD) (Figure S3A). By contrast, total ROS levels nearly doubled upon cytokine treatment of control islets (Figures 4A, 4B, and S3A) and in those treated with the non-GK-activating BAD BH3 mutant either in the form of a stapled peptide (BAD $SAHB_A$ AAA; Figures 4A and 4B) or the corresponding full-length BAD mutant protein (BAD AAA; Figure S3A) (Danial et al., 2008; Fu et al., 2020; Giménez-Cassina et al., 2014; Ljubicic et al., 2015). These data indicate that the antioxidant benefits of phospho-BAD mimicry require its GK-activating capacity, which is consistent with published observations that *GK* knockdown blocks the survival-promoting effects of phospho-BAD in islets exposed to various death stimuli, including pro-inflammatory cytokines (Fu et al., 2020; Ljubicic et al., 2015).

The observation that phospho-BAD mimicry has antioxidant effects in both human and mouse islets is especially noteworthy considering that human islets have a functional nicotinamide nucleotide transhydrogenase (NNT) enzyme, which is not expressed in islets derived from C57BL/6J mice used in these experiments. This suggests that NNT activity and its modulation of NADPH levels do not influence the outcome of phospho-BAD mimicry in this setting. However, to directly rule out this possibility, we also quantified ROS levels in NNT-expressing islets derived from C57BL/6N mice and found comparable ROS-diminishing and protective effects by phospho-BAD mimicry to those seen in C57BL/6J islets (Figures S3B and S3C).

To directly test the contribution of *de novo* GSH synthesis to differences in ROS levels in the absence or presence of phospho-BAD mimicry, we interfered with the rate-limiting enzyme of GSH synthesis, glutamate-cysteine ligase (GCL), also known as γ-glutamylcysteine synthase, by short hairpin RNA (shRNA)-mediated depletion of its catalytic subunit (GCLC) or pharmacologic inhibition using buthionine sulfoximine (BSO) (Bailey et al., 1994; Griffith, 1982; Griffith and Meister, 1979). Both approaches block the capacity of phospho-BAD mimicry to restrain ROS accumulation and protect islets from inflammation toxicity (Figures 4C–4F and S3D). Thus, activation of GSH synthesis is part of the metabolic mechanism underlying the antioxidant effects of the BAD-GK axis.

gamma-glutamylcyclotransferase; GGT, gamma-glutamyltransferase; GNMT, glycine N-methyltransferase; GPX, GSH peroxidase; GSS, GSH synthase; GSR, GSH-disulfide reductase; KYAT, kynurenine aminotransferase; MAT, methionine adenosyltransferase; OPLAH, 5-oxoprolinase ATP-hydrolyzing; PSPH, phosphoserine phosphatase; SAH, S-adenosylhomocysteine.

Data are represented as means ± SEM. Statistical analyses are one-way ANOVAs with comparisons of cytokine-treated cells to PBS control.

See also Figure S1 and Tables S1 and S2.

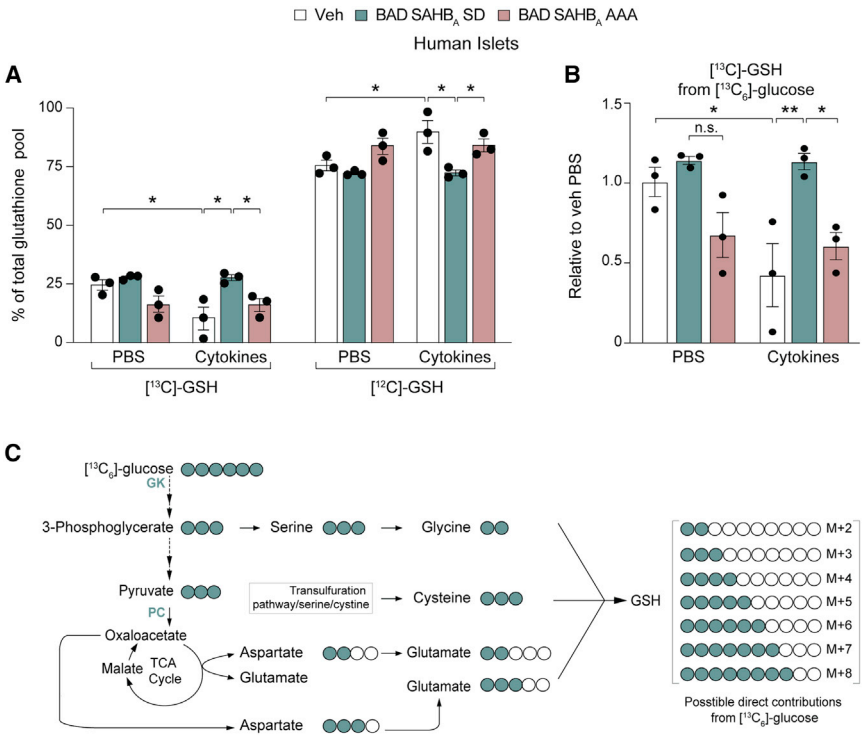

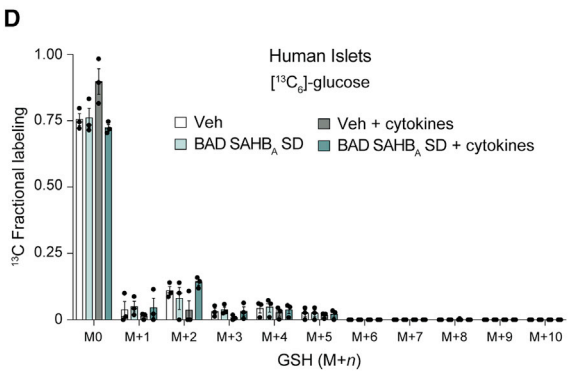

Figure 2. Glucose metabolism supports GSH synthesis in human islets

(A) Glucose-tracing studies in human islets measuring total ^{13}C incorporation from [^{13}C$_6$]-glucose into GSH [^{13}C]-GSH and unlabeled GSH, [^{12}C]-GSH. Human islets were treated with veh, BAD SAHB$_A$ SD, or BAD SAHB$_A$ AAA in the presence of PBS or a pro-inflammatory cytokine cocktail (TNF-α, IL-1β, and IFNγ) and labeled in RPMI containing 5.8 mM [^{13}C$_6$]-glucose for 24 h (n = 3).

(B) Relative labeling of [^{13}C]-GSH out of the total sum of GSH pool [^{13}C+^{12}C] from experiment in (A) normalized to veh PBS.

(C) Potential labeling routes and resultant GSH isotopologs from [^{13}C$_6$]-glucose. Only isotopologs from direct incorporation routes are shown without considering multiple rounds of synthesis, recycling steps of GSH, and/or label dilution.

(D) Non-normalized total fractional labeling for each mass isotopolog of GSH (M+n), including unlabeled GSH (M+0), quantified in experiment (A). Data are represented as means ± SEM. *p < 0.05; **p < 0.005; n.s., non-significant via two-way ANOVA with Tukey's adjustment for multiple comparisons.

PC protects against oxidative stress triggered by inflammation

PC activity is reduced in islets treated with pro-inflammatory cytokines, and maintaining PC activity by PC overexpression or phospho-BAD mimicry protects against inflammation toxicity (Fu et al., 2020). This is mediated, in part, by PC-directed ureagenesis, which reduces NO synthesis in response to pro-inflammatory cytokines. We previously mapped the ureagenic effects of PC to its support of aspartate production and the activity of the aspartate-argininosuccinate shunt and urea cycle (Fu et al., 2020). PC-mediated anaplerosis can provide additional protective mechanisms to counter oxidative and nitrosative stress in this setting by activating transmitochondrial pyruvate cycles that generate NADPH relevant for thioredoxin and GSH antioxidant pathways (Cappel et al., 2019; Heart et al., 2009; Jensen et al., 2008; Jitrapakdee et al., 2010; MacDonald et al., 2005; Prentki et al., 2013; Stancill et al., 2019).

In light of these considerations, PC depletion reversed the ROS-attenuating effect of phospho-BAD mimicry in human and mouse islets treated with pro-inflammatory cytokines, while expression of an shRNA-resistant PC cDNA restored this effect (Figures 5A, 5B, S4A, and S4B).

The outcome of PC modulation on ROS may be explained by its effect on cytosolic NADPH/NADP$^+$ as previously reported in multiple cell types (Cappel et al., 2019; Li et al., 2016; Wilmanski et al., 2017; Xu et al., 2008); however, a role for PC in GSH biosynthesis cannot be excluded. This is further supported by the observation that boosting GSH synthesis by supplementing PC-depleted human islets with the cysteine analog *N*-acetylcysteine (NAC) diminished ROS levels and protected PC-depleted islets from inflammation toxicity (Figures 5C and S4C). Importantly, metabolic tracing studies underscored the functional requirement of PC for glucose contribution to GSH synthesis. Specifically, *PC* knockdown in human islets significantly diminished the effect of phospho-BAD mimicry on M+2 GSH in the presence of cytokines (Figures 5D, 5E, and S4D).

We next undertook gain- and loss-of-function approaches to assess whether alterations in PC, independent of phospho-BAD mimicry, are sufficient to modulate ROS levels in human islets. Depletion of PC exacerbates ROS accumulation in islets undergoing inflammation stress, which can be reversed by NAC treatment (Figure 5F). Conversely, PC overexpression is sufficient to diminish cytokine-induced increases in ROS and protects islets from inflammation toxicity (Figures 5G and 5H).

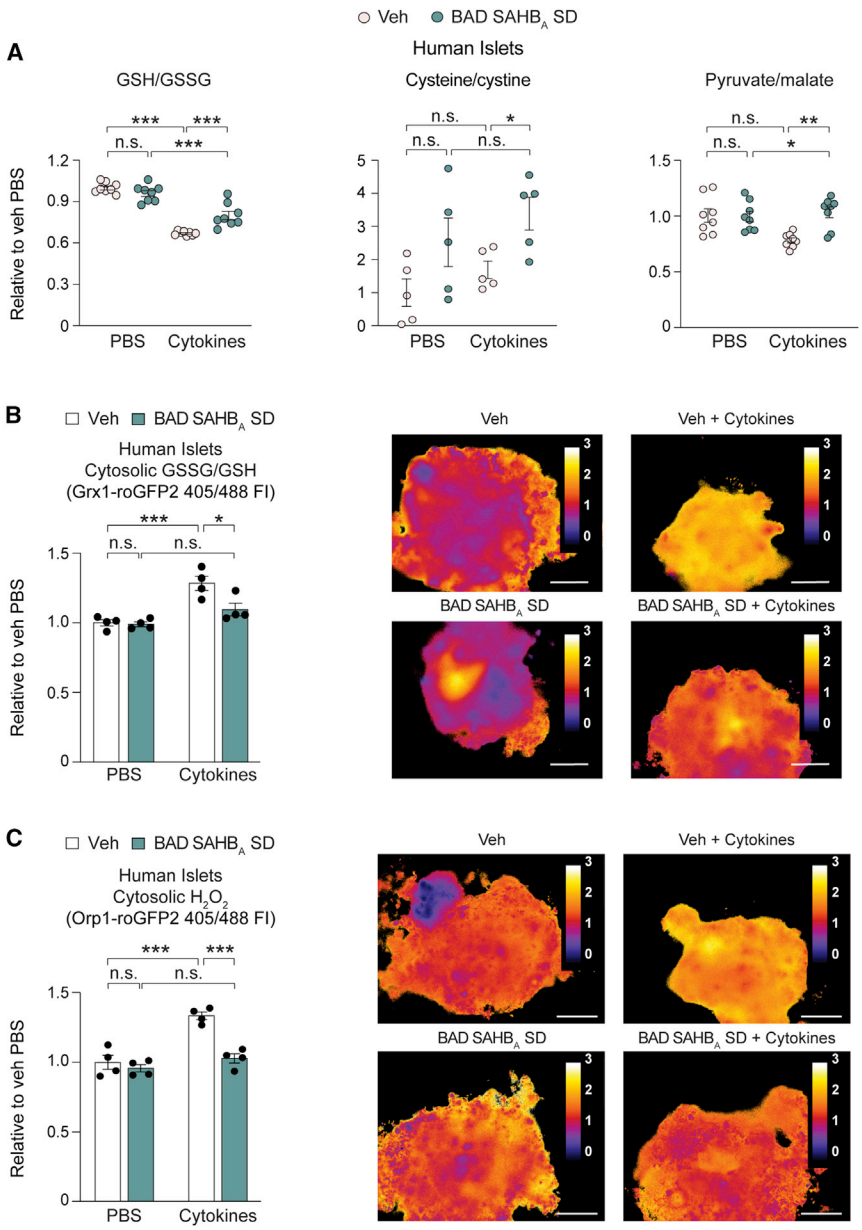

Figure 3. The effect of phospho-BAD mimicry on redox coupling in human islets undergoing inflammation stress

(A) Ratios of GSH/GSSG, cysteine/cystine, and pyruvate/malate measured as in Figure 1.

(B) Quantification (left) and representative images (right) of ratiometric fluorescence intensity in re-aggregated human islets expressing cytosolic Grx1-roGFP2 that were treated with veh or BAD SAHB$_A$ SD in the presence of PBS or cytokines for 24 h (n = 4). Scale bars, 100 μm at 20× magnification to capture the entire re-aggregated islet without subcellular resolution. Ratiometric images were generated by dividing images captured at 405 nm (oxidized) by those taken at 488 nm (reduced), thus keeping spatial information of the ratio intensities and applying an arbitrary color intensity scale onto the calculated images.

(C) Quantification (left) and representative images (right) of ratiometric fluorescence intensity in re-aggregated human islets expressing cytosolic Orp1-roGFP2 that were treated with veh or BAD SAHB$_A$ SD in the presence of PBS or cytokines for 24 h (n = 4). Image outputs calculations were performed as in (B).

Data are represented as means ± SEM. *$p < 0.05$; **$p < 0.005$; ***$p < 0.0005$; n.s., non-significant via two-way ANOVA with Tukey's adjustment for multiple comparisons.

See also Figure S2.

Moreover, pharmacologic inhibition of GCL by BSO blocked the protective effect of PC (Figure 5H). Taken together, these data indicate that GSH synthesis is relevant for PC's capacity to restrain ROS accumulation and cell death during islet inflammation.

PC is required for maintenance of GSH pools and protection from nitrosative stress

We have recently shown that PC activation alone as well as phospho-BAD mimicry reduces NO synthesis in the presence of pro-inflammatory cytokines by shifting arginine utilization to urea synthesis (Fu et al., 2020). As such, both dampened NO synthesis and increased antioxidant capacity by PC overexpression or phospho-BAD mimicry are predicted to lower ROS accumulation in response to pro-inflammatory cytokines, making it difficult to specifically distill the role of enhanced reductive potential. To sidestep this scenario, we treated islets with the NO donor GEA3162, essentially bypassing the effect of PC or phospho-BAD mimicry on NO synthesis. In the presence of the NO donor, BAD SAHB$_A$ SD-treated islets maintained a larger GSH pool and a higher GSH/GSSG ratio (Figure 6A). This was further consistent with lower ROS levels and higher viability in this setting (Figures 6B and 6C). The effect of BAD SAHB$_A$ SD on abating oxidative stress requires its GK-activating capacity as BAD SAHB$_A$ AAA did not show the same effect (Figure 6B). ROS accumulation was similarly reduced in islets expressing the full-length BAD SD phospho-mimic mutant exposed to the NO donor (Figure 6D). Importantly, BSO treatment reversed the protective effect of phospho-BAD mimicry on NO-induced changes in ROS and cell death, indicating the requirement of *de novo* GSH synthesis (Figures 6C and 6D).

We next tested the functional contribution of PC to enhanced GSH levels in islets subjected to phospho-BAD mimicry and exposed to nitrosative stress. Genetic depletion of PC weakens the ROS-diminishing and survival-promoting capacity of phospho-BAD mimicry in human islets exposed to NO donor (Figures 6E and 6F). Importantly, we also tested the functional

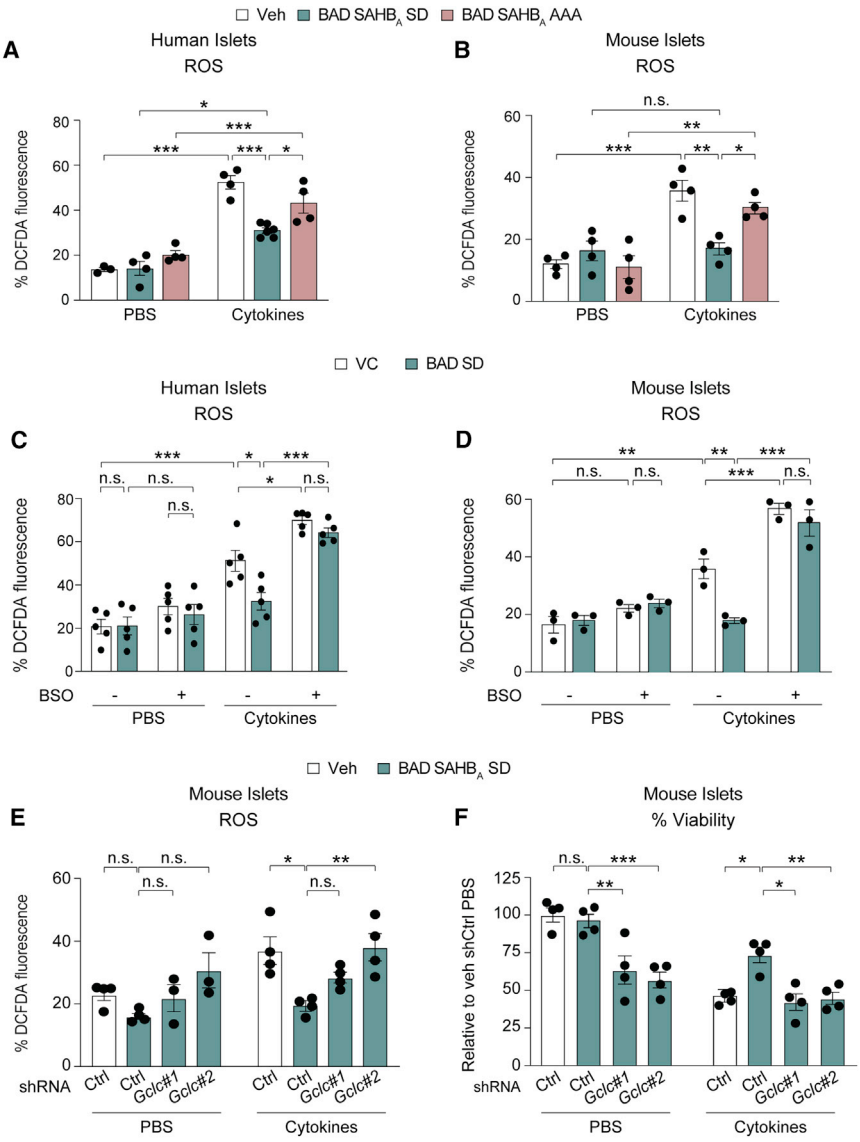

Figure 4. The BAD-GK axis restrains inflammation-induced ROS accumulation by supporting GSH synthesis

(A and B) ROS levels measured as %2',7'-dichlorodihydrofluorescein diacetate (DCFDA)-positive cells normalized to the maximal signal determined with H_2O_2 in veh-, BAD SAHB$_A$ SD-, or BAD SAHB$_A$ AAA-treated human (A) and mouse (B) islets cultured in the presence of PBS or cytokines for 24 h (n = 4).

(C and D) ROS levels in human (C) and mouse (D) islets expressing vector control (VC) or BAD SD that were treated for 24 h with PBS or cytokines in the presence or absence of BSO (n = 5, and n = 3, respectively).

(E) ROS levels in mouse islets subjected to *GCLC* knockdown using two independent shRNAs and treated with veh or BAD SAHB$_A$ SD in the presence of PBS or cytokines for 24 h (n = 4).

(F) Viability of mouse islets subjected to phospho-BAD mimicry and *GCLC* knockdown as in (E) and treated with cytokines for 48 h. Viability was assessed by flow cytometric measurement of Annexin V/7-Aminoactinomycin D (7AAD) incorporation (n = 4).

Data are represented as means ± SEM. *p < 0.05; **p < 0.005; ***p < 0.0005; n.s., non-significant via two-way ANOVA with Tukey's adjustment for multiple comparisons. Glucose concentration was 5.8 mM in PIM(S) media for all human islet cultures and 11 mM in RPMI for all mouse islet cultures. See also Figure S3.

contribution of PC to GSH independent of phospho-BAD mimicry and found that genetic depletion of PC in human islets is sufficient to reduce the pool of GSH and GSH/GSSG ratio under nitrosative stress (Figure 6G), supporting a role for this anaplerotic enzyme in maintaining cellular GSH pools.

DISCUSSION

PC-associated trans-mitochondrial pyruvate cycles are an important source of NADPH and additional metabolic coupling factors in β cells relevant for insulin release in response to acute stimulation with glucose or other fuels (Jensen et al., 2008; Jitrapakdee et al., 2010; MacDonald et al., 2005; Prentki et al., 2013). Accordingly, silencing of *PC* in rodent islets and insulinoma cells decreases the NADPH/NADP$^+$ ratio and inhibits insulin secretion (Xu et al., 2008). Yet, if and how PC influences the β cell response to oxidative stress has not been directly investigated. Our observation that GSH/GSSG ratio is diminished upon chemical or genetic inhibition of PC in human donor islets undergoing nitrosative/oxidative stress is consistent with PC's effects on NADPH/NADP$^+$ ratios. However, we find that the ROS-diminishing effect of PC additionally involves a previously unappreciated role in *de novo* GSH synthesis beyond changes in NADPH/NADP$^+$ ratio. First, interference with PC in human islets attenuates the contribution of glucose carbons to GSH synthesis. Second, the ROS-diminishing effect of PC in human islets undergoing inflammation is significantly impaired when the rate-limiting enzyme of *de novo* GSH synthesis is inhibited via pharmacologic or genetic means. Third, the consequence of *PC* knockdown on ROS accumulation is associated with reduced GSH pools and is reversed by supplementation with NAC. And fourth, under conditions where increased glucose metabolism imparts antioxidant effects via PC as in phospho-BAD mimicry, GSH pools are increased and inhibition of *de novo* GSH synthesis interferes with the protective effects of glucose metabolism. Thus, the metabolic input from glucose and PC converges on the GSH system not only at the level of NADPH but also at the level of GSH biosynthesis to abate ROS accumulation during inflammatory and oxidative stress (Figure 6H). To our knowledge, this is the

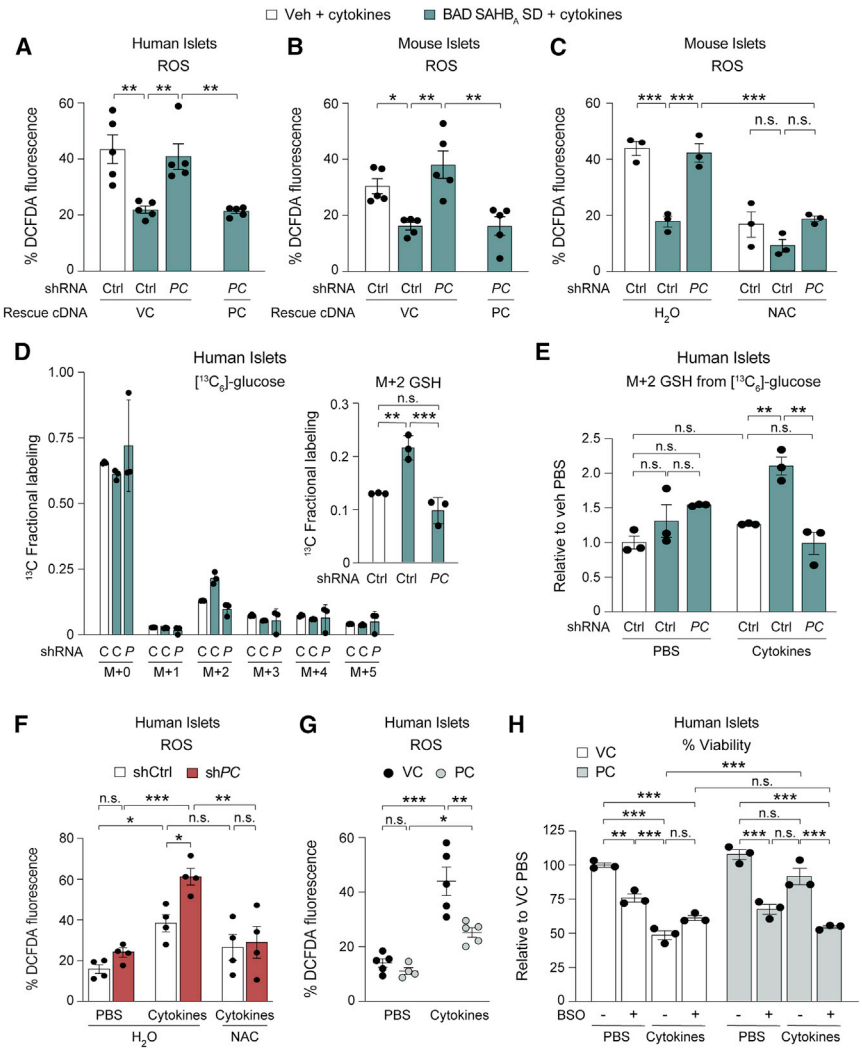

Figure 5. PC protects against oxidative stress triggered by inflammation

(A and B) The effect of *PC* knockdown on ROS levels in human (A) and mouse (B) islets treated with veh or BAD SAHB$_A$ SD and cultured in the presence of cytokines for 24 h. Rescue with shRNA-resistant PC cDNA (PC) compared with VC validates the on-target effects of *PC* shRNA (n = 5).

(C) Quantification of ROS levels in mouse islets treated as in (B) in the presence of *N*-acetylcysteine (NAC) or veh for NAC (H$_2$O). Values are normalized to PBS-treated shRNA control samples (shCtrl) (n = 3).

(D) Quantification of [^{13}C$_6$]-glucose-derived GSH as non-normalized total fractional labeling for each mass isotopolog of GSH (M+n), including unlabeled GSH (M+0). Human islets were treated with veh or BAD SAHB$_A$ SD and transduced with control (Ctrl) or *PC* shRNA lentiviruses in the presence of cytokines and labeled in media containing 5.8 mM [^{13}C$_6$]-glucose for 24 h (n = 3). Inset magnifies the quantification of M+2 GSH. C and *P* on the y axis denote Ctrl and *PC* knockdown, respectively.

(E) Relative labeling of [^{13}C]-GSH out of the total sum of GSH pool [^{13}C+^{12}C] from experiment in (D) normalized to veh PBS.

(F) ROS levels in human islets transduced with lentiviruses carrying Ctrl or *PC* shRNA and treated with PBS or cytokines in the absence (H$_2$O) or presence of NAC (n = 4).

(G) ROS levels in human islets transduced with VC- or human PC (PC)-expressing lentiviruses in the presence of PBS or cytokines for 24 h (n = 5).

(H) The effect of PC overexpression on the viability of human islets treated with cytokines for 48 h and its reversal upon inhibition of GSH synthesis with BSO. Values are shown relative to VC PBS samples (n = 3).

Data are represented as means ± SEM. *p < 0.05; **p < 0.005; ***p < 0.0005; n.s., non-significant via one-way (A and B) or two-way (C–H) ANOVA with Tukey's adjustment for multiple comparisons.

See also Figure S4.

first evidence that PC and glucose metabolism direct GSH synthesis in islets subjected to diabetes-associated stress stimuli.

Synthesis of the tripeptide GSH (γ-glutamyl-cysteinyl-glycine) is dependent on-precursor amino acids glutamate, cysteine, and glycine, which may be taken up from media or synthesized intracellularly, as well as the rate-limiting enzyme GCL. Numerous studies have utilized metabolic tracing via glutamine and glutamate to examine *de novo* GSH synthesis in multiple cell types; however, little is known about the biosynthetic input from glucose into this anabolic pathway. Considering the multitude of metabolic paths to biosynthetic precursors of GSH, the finding that glucose carbons normally enrich ~25% of total GSH pool in human islets is remarkable. Furthermore, phospho-BAD mimicry supports a larger contribution from glucose to GSH synthesis in islets undergoing inflammation stress. This benefit is mediated by PC and requires the GK-activating capacity of phospho-BAD mimicry. Our tracing studies further revealed that the M+2 GSH is the predominant isotopolog containing glucose carbons. One possible route producing M+2 GSH is via precursor glutamate, which may result from incorporation of M+2 glutamate from [^{13}C$_6$]-glucose in the first round of the TCA cycle (Figure 2C). Interestingly, glutamate is enriched in human islets protected from inflammation by phospho-BAD mimicry (Figure 1) and is in direct exchange with aspartate, which is increased by PC in human islets undergoing inflammation stress (Fu et al., 2020). However, alternative paths to M+2 GSH cannot be ruled out and the definitive origin of this PC-dependent labeling pattern awaits future studies.

The observation that PC is required for glucose input into GSH biosynthesis predicts that the status of PC activity may be an important determinant of whether increases in glucose metabolism will impart protective or toxic effects in stressed β cells. Within this context, we have previously shown that supraphysiologic increases in glucose metabolism as in genetic or pharmacologic activation of GK at its allosteric site, which drastically lower the enzyme's K_M for glucose, are associated

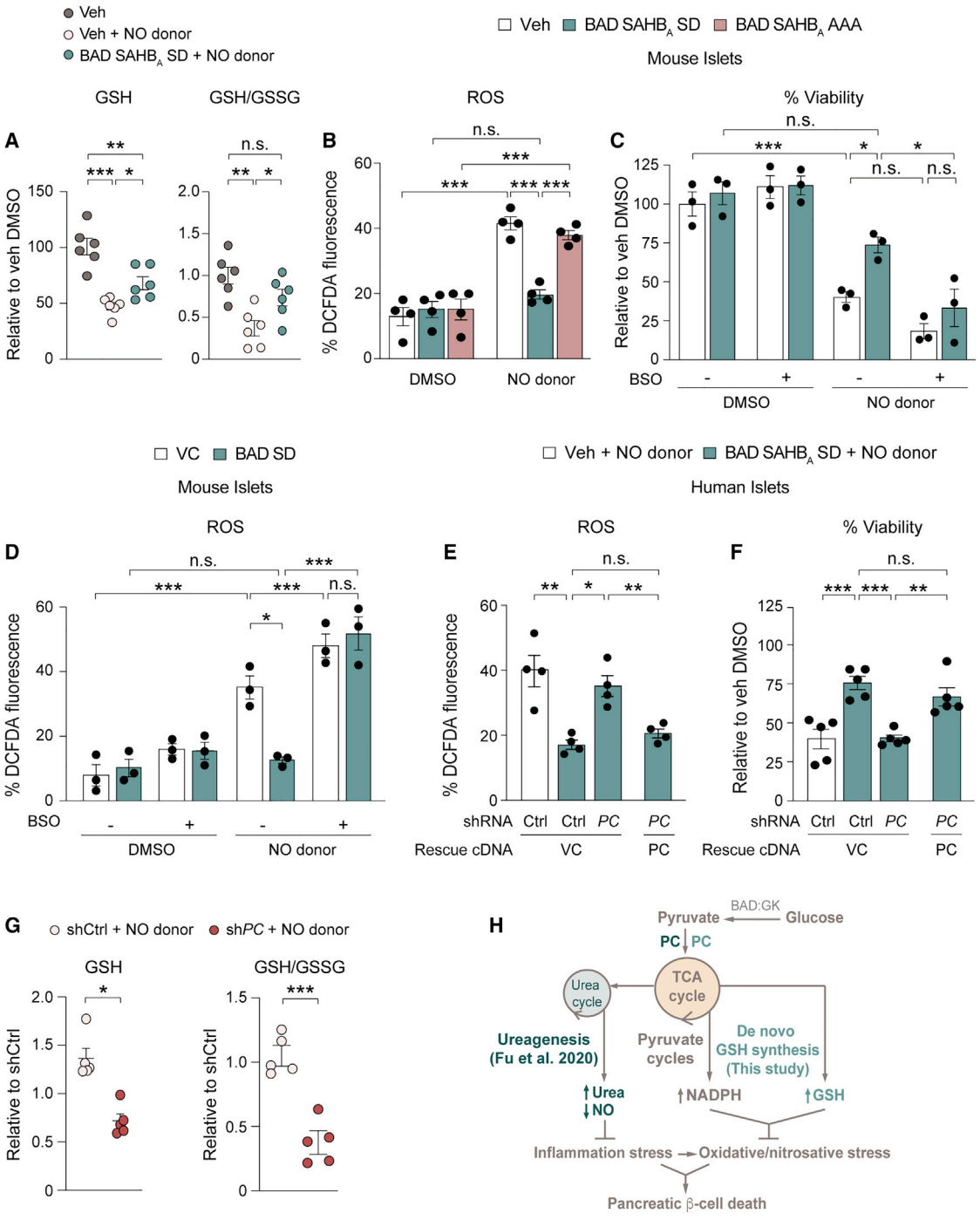

Figure 6. PC is required for maintenance of GSH pools and protection from nitrosative stress

(A) GSH levels and GSH/GSSG ratios in vehicle- and BAD SAHB$_A$ SD-treated mouse islets exposed to the NO donor (GEA3162 dissolved in DMSO) for 24 h as measured by quantitative colorimetric assays. Data are normalized to protein levels with vehicle DMSO set to 100% (n = 6).

(B) ROS levels in mouse islets treated with veh, BAD SAHB$_A$ SD, or BAD SAHB$_A$ AAA and cultured in the presence of the NO donor for 24 h (n = 4).

(C) Viability of mouse islets treated with the indicated compounds followed by 48 h of cytokine treatment in the absence or presence of BSO (n = 3).

(D) ROS levels in islets expressing VC or BAD SD treated as in (C) (n = 3).

(E and F) The effect of *PC* knockdown on ROS (E) and viability (F) of human islets treated with the NO donor for 24 h (E) or 48 h (F). Rescue with shRNA-resistant PC cDNA validates the on-target effects of *PC* shRNA (n = 4 and n = 5 for ROS and viability measurements, respectively).

(G) The effect of *PC* knockdown on GSH levels and GSH/GSSG ratios in human islets exposed to the NO donor for 24 h as measured by mass spectrometry. Values are relative to vehicle DMSO-treated islets set to 1 (n = 5).

(legend continued on next page)

with reduced PC activity in stressed islets and do not protect β cells (Fu et al., 2020). This non-protective mode of GK activation resembles glucotoxic conditions as in chronic exposure to high glucose mimicking the diabetic milieu, which can be reversed by PC overexpression (Fu et al., 2020). In comparison, increases in glucose metabolism via the BAD-GK pathway occur while preserving the native physiologic affinity of GK for glucose and are associated with higher PC activity and protection of β cells from stress (Fu et al., 2020). Thus, PC may serve as a control point whether increases in glucose metabolism will have damaging or beneficial outcomes in that its impairment diminishes the protective effects of glucose in the face of inflammatory, nitrosative, and oxidative stress. The mechanism whereby PC activity is differentially regulated in response to these two kinetically distinguishable modes of GK activation likely involves a combination of differences in PC allosteric regulation and substrate availability, which is under active investigation.

Overall, our findings using both phospho-BAD mimicry to model the protective glucose-PC pathway as well as *PC* overexpression or knockdown approaches, independent of BAD modifications, point to a multi-faceted PC-dependent pro-survival program in human and rodent islets. Beyond protective ureagenesis (Fu et al., 2020), this anabolic program also includes *de novo* GSH synthesis (Figure 6H). This dual defense mechanism is particularly intriguing given that it involves reduced NO production as a consequence of increased ureagenesis (Fu et al., 2020) as well as increased antioxidant capacity via enhanced GSH synthesis and redox coupling, allowing cells to simultaneously control generation and clearance of oxidative/nitrosative stress. Such PC-driven protective mechanisms, together with PC's prominence in fuel-stimulated insulin secretion, make this TCA cycle enzyme an attractive metabolic hub for regulation of functional β cell mass, including its potential benefit in islet transplantation and in enhancing the resilience of stem cell-derived β cells to inflammatory and oxidative stress.

Limitations of the study

A limitation of this investigation is the lack of conclusive identification of the specific precursor metabolite(s) for GSH biosynthesis that is/are enriched by glucose carbons in a PC-dependent manner. This was due to limitations in human donor islet material and detection limits for simultaneous measurements of all potential glucose-labeled intermediates along the GSH synthesis pathway within a sample, which require further optimization. Nonetheless, our tracer studies indicate substantial contribution from glucose and PC to GSH pools in human islets. In addition, if and how PC-dependent GSH synthesis functions as a protective axis in other islet cell types such as α cells remains to be determined. Addressing this question will also require a better understanding of dynamics of glucose flux in α and β cells using islet cell-type-specific tools and models.

STAR★METHODS

Detailed methods are provided in the online version of this paper and include the following:

- KEY RESOURCES TABLE
- RESOURCE AVAILABILITY
  - Lead contact
  - Materials availability
  - Data and code availability
- EXPERIMENTAL MODEL AND SUBJECT DETAILS
  - Human islets
  - Mouse islets
- METHOD DETAILS
  - Islet culture, cytokine and NO donor treatment
  - SAHB synthesis and treatment
  - Untargeted metabolomics
  - Targeted metabolomics by LC-MS/MS
  - Detection of GSH/GSSG by colorimetric assay
  - Genetic manipulation of islets
  - Quantification of ROS and cell survival by flow cytometry
  - Islet re-aggregation, biosensor expression and quantification of Grx1- and Orp1-roGFP2 fluorescence
- QUANTIFICATION AND STATISTICAL ANALYSIS
  - Metabolomics data and statistical analysis

SUPPLEMENTAL INFORMATION

Supplemental information can be found online at https://doi.org/10.1016/j.celrep.2021.110037.

ACKNOWLEDGMENTS

We thank Adolfo Garcia-Ocaña and members of the Danial laboratory for helpful discussions. This work was supported by the US NIH grants R01DK078081 (N.N.D.), R35CA197583 (L.D.W.), R50CA211399 (G.H.B.), R01DK123095 (E.T.C.), and R01AA026914 (M.L.-R.); Juvenile Diabetes Research Foundation grant 2-SRA-2015-58-Q-R (N.N.D.); Barry and Mimi Sternlicht Type 1 Diabetes Research Fund (N.N.D.); Qatar Biomedical Research Institute and Harvard Stem Cell Institute Joint Research Program (N.N.D.); the Claudia Adams Barr Program (E.T.C.); the Lavine Family Fund (E.T.C.); and the Pew Charitable Trust (E.T.C.). A.F. was supported by a postdoctoral fellowship from the Juvenile Diabetes Research Foundation (JDRF). The Integrated Islet Distribution Program (IIDP) is supported by NIH grant 2UC4DK098085. The Rosalind and Morris Goodman Cancer Institute, Metabolomics Innovation Resource facility is supported by the Canada Foundation for Innovation, Dr. John R. and Clara M. Fraser Memorial Trust, and the Terry Fox Foundation in partnership with the Foundation du Cancer du Sein du Quebec and McGill University. A.M.J.S. is a fellow of the Royal Society of Canada and is supported through a Canada Research Chair in Regenerative Medicine and Transplantation Surgery.

AUTHOR CONTRIBUTIONS

Conceptualization, A.F. and N.N.D.; methodology, D.A., A.R., E.T.C., M.L.-R., A.F., and N.N.D.; investigation, L.v.R., L.E., N.A., D.A., A.F., and N.N.D.; writing – original draft, A.F. and N.N.D.; writing – review & editing, A.F., D.A., G.H.B., M.L.-R., A.M.J.S., and N.N.D.; funding acquisition, G.H.B.,

(H) Protective effects of BAD:GK:PC axis in countering inflammation and oxidative/nitrosative stress.
Data are represented as means ± SEM. *$p < 0.05$; **$p < 0.005$; ***$p < 0.0005$; n.s., non-significant via one-way ANOVA (A, B, and E–G) or two-way ANOVA (C and D) with Tukey's adjustment for multiple comparisons.

L.D.W., A.M.J.S., A.F., and N.N.D.; resources, T.K., G.H.B., M.L.-R., L.D.W., and A.M.J.S.; supervision, A.F. and N.N.D.

DECLARATIONS OF INTERESTS

L.D.W. is a scientific co-founder and shareholder in Aileron Therapeutics. M.L.-R. is a co-founder and consultant of Enspire Bio. E.T.C. is a founder, board member, and equity holder in EoCys Therapeutics.

Received: January 11, 2021
Revised: August 25, 2021
Accepted: November 1, 2021
Published: November 23, 2021

REFERENCES

Bailey, H.H., Mulcahy, R.T., Tutsch, K.D., Arzoomanian, R.Z., Alberti, D., Tombes, M.B., Wilding, G., Pomplun, M., and Spriggs, D.R. (1994). Phase I clinical trial of intravenous L-buthionine sulfoximine and melphalan: an attempt at modulation of glutathione. J. Clin. Oncol. *12*, 194–205.

Bensellam, M., Laybutt, D.R., and Jonas, J.C. (2012). The molecular mechanisms of pancreatic β-cell glucotoxicity: recent findings and future research directions. Mol. Cell. Endocrinol. *364*, 1–27.

Brereton, M.F., Rohm, M., Shimomura, K., Holland, C., Tornovsky-Babeay, S., Dadon, D., Iberl, M., Chibalina, M.V., Lee, S., Glaser, B., et al. (2016). Hyperglycaemia induces metabolic dysfunction and glycogen accumulation in pancreatic β-cells. Nat. Commun. *7*, 13496.

Cappel, D.A., Deja, S., Duarte, J.A.G., Kucejova, B., Iñigo, M., Fletcher, J.A., Fu, X., Berglund, E.D., Liu, T., Elmquist, J.K., et al. (2019). Pyruvate-Carboxylase-Mediated Anaplerosis Promotes Antioxidant Capacity by Sustaining TCA Cycle and Redox Metabolism in Liver. Cell Metab. *29*, 1291–1305.e8.

Dadon, D., Tornovsky-Babaey, S., Furth-Lavi, J., Ben-Zvi, D., Ziv, O., Schyr-Ben-Haroush, R., Stolovich-Rain, M., Hija, A., Porat, S., Granot, Z., et al. (2012). Glucose metabolism: key endogenous regulator of β-cell replication and survival. Diabetes Obes. Metab. *14* (*Suppl 3*), 101–108.

Danial, N.N., Walensky, L.D., Zhang, C.Y., Choi, C.S., Fisher, J.K., Molina, A.J., Datta, S.R., Pitter, K.L., Bird, G.H., Wikstrom, J.D., et al. (2008). Dual role of proapoptotic BAD in insulin secretion and beta cell survival. Nat. Med. *14*, 144–153.

Donath, M.Y., Dalmas, É., Sauter, N.S., and Böni-Schnetzler, M. (2013). Inflammation in obesity and diabetes: islet dysfunction and therapeutic opportunity. Cell Metab. *17*, 860–872.

Eizirik, D.L., Colli, M.L., and Ortis, F. (2009). The role of inflammation in insulitis and beta-cell loss in type 1 diabetes. Nat. Rev. Endocrinol. *5*, 219–226.

Fu, A., Alvarez-Perez, J.C., Avizonis, D., Kin, T., Ficarro, S.B., Choi, D.W., Karakose, E., Badur, M.G., Evans, L., Rosselot, C., et al. (2020). Glucose-dependent partitioning of arginine to the urea cycle protects β-cells from inflammation. Nat. Metab. *2*, 432–446.

Fuhrer, T., Heer, D., Begemann, B., and Zamboni, N. (2011). High-throughput, accurate mass metabolome profiling of cellular extracts by flow injection-time-of-flight mass spectrometry. Anal. Chem. *83*, 7074–7080.

Gerber, P.A., and Rutter, G.A. (2017). The Role of Oxidative Stress and Hypoxia in Pancreatic Beta-Cell Dysfunction in Diabetes Mellitus. Antioxid. Redox Signal. *26*, 501–518.

Giménez-Cassina, A., Garcia-Haro, L., Choi, C.S., Osundiji, M.A., Lane, E.A., Huang, H., Yildirim, M.A., Szlyk, B., Fisher, J.K., Polak, K., et al. (2014). Regulation of hepatic energy metabolism and gluconeogenesis by BAD. Cell Metab. *19*, 272–284.

Griffith, O.W. (1982). Mechanism of action, metabolism, and toxicity of buthionine sulfoximine and its higher homologs, potent inhibitors of glutathione synthesis. J. Biol. Chem. *257*, 13704–13712.

Griffith, O.W., and Meister, A. (1979). Potent and specific inhibition of glutathione synthesis by buthionine sulfoximine (S-n-butyl homocysteine sulfoximine). J. Biol. Chem. *254*, 7558–7560.

Gutscher, M., Pauleau, A.L., Marty, L., Brach, T., Wabnitz, G.H., Samstag, Y., Meyer, A.J., and Dick, T.P. (2008). Real-time imaging of the intracellular glutathione redox potential. Nat. Methods *5*, 553–559.

Gutscher, M., Sobotta, M.C., Wabnitz, G.H., Ballikaya, S., Meyer, A.J., Samstag, Y., and Dick, T.P. (2009). Proximity-based protein thiol oxidation by H2O2-scavenging peroxidases. J. Biol. Chem. *284*, 31532–31540.

Heart, E., Cline, G.W., Collis, L.P., Pongratz, R.L., Gray, J.P., and Smith, P.J. (2009). Role for malic enzyme, pyruvate carboxylation, and mitochondrial malate import in glucose-stimulated insulin secretion. Am. J. Physiol. Endocrinol. Metab. *296*, E1354–E1362.

Jensen, M.V., Joseph, J.W., Ronnebaum, S.M., Burgess, S.C., Sherry, A.D., and Newgard, C.B. (2008). Metabolic cycling in control of glucose-stimulated insulin secretion. Am. J. Physiol. Endocrinol. Metab. *295*, E1287–E1297.

Jitrapakdee, S., Wutthisathapornchai, A., Wallace, J.C., and MacDonald, M.J. (2010). Regulation of insulin secretion: role of mitochondrial signalling. Diabetologia *53*, 1019–1032.

Levitt, H.E., Cyphert, T.J., Pascoe, J.L., Hollern, D.A., Abraham, N., Lundell, R.J., Rosa, T., Romano, L.C., Zou, B., O'Donnell, C.P., et al. (2011). Glucose stimulates human beta cell replication in vivo in islets transplanted into NOD-severe combined immunodeficiency (SCID) mice. Diabetologia *54*, 572–582.

Li, X., Cheng, K.K.Y., Liu, Z., Yang, J.K., Wang, B., Jiang, X., Zhou, Y., Hallenborg, P., Hoo, R.L.C., Lam, K.S.L., et al. (2016). The MDM2-p53-pyruvate carboxylase signalling axis couples mitochondrial metabolism to glucose-stimulated insulin secretion in pancreatic β-cells. Nat. Commun. *7*, 11740.

Ljubicic, S., Polak, K., Fu, A., Wiwczar, J., Szlyk, B., Chang, Y., Alvarez-Perez, J.C., Bird, G.H., Walensky, L.D., Garcia-Ocaña, A., and Danial, N.N. (2015). Phospho-BAD BH3 mimicry protects β cells and restores functional β cell mass in diabetes. Cell Rep. *10*, 497–504.

Lytrivi, M., Castell, A.L., Poitout, V., and Cnop, M. (2020). Recent Insights Into Mechanisms of β-Cell Lipo- and Glucolipotoxicity in Type 2 Diabetes. J. Mol. Biol. *432*, 1514–1534.

MacDonald, P.E., Joseph, J.W., and Rorsman, P. (2005). Glucose-sensing mechanisms in pancreatic beta-cells. Philos. Trans. R. Soc. Lond. B Biol. Sci. *360*, 2211–2225.

Metukuri, M.R., Zhang, P., Basantani, M.K., Chin, C., Stamateris, R.E., Alonso, L.C., Takane, K.K., Gramignoli, R., Strom, S.C., O'Doherty, R.M., et al. (2012). ChREBP mediates glucose-stimulated pancreatic β-cell proliferation. Diabetes *61*, 2004–2015.

Miki, A., Ricordi, C., Sakuma, Y., Yamamoto, T., Misawa, R., Mita, A., Molano, R.D., Vaziri, N.D., Pileggi, A., and Ichii, H. (2018). Divergent antioxidant capacity of human islet cell subsets: A potential cause of beta-cell vulnerability in diabetes and islet transplantation. PLoS ONE *13*, e0196570.

Morgan, B., Sobotta, M.C., and Dick, T.P. (2011). Measuring E(GSH) and H2O2 with roGFP2-based redox probes. Free Radic. Biol. Med. *51*, 1943–1951.

Newsholme, P., Keane, K.N., Carlessi, R., and Cruzat, V. (2019). Oxidative stress pathways in pancreatic β-cells and insulin-sensitive cells and tissues: importance to cell metabolism, function, and dysfunction. Am. J. Physiol. Cell Physiol. *317*, C420–C433.

Padgett, L.E., Broniowska, K.A., Hansen, P.A., Corbett, J.A., and Tse, H.M. (2013). The role of reactive oxygen species and proinflammatory cytokines in type 1 diabetes pathogenesis. Ann. N Y Acad. Sci. *1281*, 16–35.

Pang, Z., Chong, J., Li, S., and Xia, J. (2020). MetaboAnalystR 3.0: Toward an Optimized Workflow for Global Metabolomics. Metabolites *10*, 186.

Petry, S.F., Sharifpanah, F., Sauer, H., and Linn, T. (2017). Differential expression of islet glutaredoxin 1 and 5 with high reactive oxygen species production in a mouse model of diabesity. PLoS ONE *12*, e0176267.

Prentice, K.J., Luu, L., Allister, E.M., Liu, Y., Jun, L.S., Sloop, K.W., Hardy, A.B., Wei, L., Jia, W., Fantus, I.G., et al. (2014). The furan fatty acid metabolite CMPF is elevated in diabetes and induces β cell dysfunction. Cell Metab. *19*, 653–666.

Prentki, M., Matschinsky, F.M., and Madiraju, S.R. (2013). Metabolic signaling in fuel-induced insulin secretion. Cell Metab. *18*, 162–185.

Roma, L.P., and Jonas, J.C. (2020). Nutrient Metabolism, Subcellular Redox State, and Oxidative Stress in Pancreatic Islets and β-Cells. J. Mol. Biol. *432*, 1461–1493.

Russo, M.S.T., Napylov, A., Paquet, A., and Vuckovic, D. (2020). Comparison of N-ethyl maleimide and N-(1-phenylethyl) maleimide for derivatization of biological thiols using liquid chromatography-mass spectrometry. Anal. Bioanal. Chem. *412*, 1639–1652.

Shalev, A. (2014). Minireview: Thioredoxin-interacting protein: regulation and function in the pancreatic β-cell. Mol. Endocrinol. *28*, 1211–1220.

Shum, M., Shintre, C.A., Althoff, T., Gutierrez, V., Segawa, M., Saxberg, A.D., Martinez, M., Adamson, R., Young, M.R., Faust, B., et al. (2021). ABCB10 exports mitochondrial biliverdin, driving metabolic maladaptation in obesity. Sci. Transl. Med. *13*, eabd1869.

Stancill, J.S., Broniowska, K.A., Oleson, B.J., Naatz, A., and Corbett, J.A. (2019). Pancreatic β-cells detoxify H_2O_2 through the peroxiredoxin/thioredoxin antioxidant system. J. Biol. Chem. *294*, 4843–4853.

Swisa, A., Glaser, B., and Dor, Y. (2017). Metabolic Stress and Compromised Identity of Pancreatic Beta Cells. Front. Genet. *8*, 21.

Szlyk, B., Braun, C.R., Ljubicic, S., Patton, E., Bird, G.H., Osundiji, M.A., Matschinsky, F.M., Walensky, L.D., and Danial, N.N. (2014). A phospho-BAD BH3 helix activates glucokinase by a mechanism distinct from that of allosteric activators. Nat. Struct. Mol. Biol. *21*, 36–42.

Taylor, E.L., Rossi, A.G., Shaw, C.A., Dal Rio, F.P., Haslett, C., and Megson, I.L. (2004). GEA 3162 decomposes to co-generate nitric oxide and superoxide and induces apoptosis in human neutrophils via a peroxynitrite-dependent mechanism. Br. J. Pharmacol. *143*, 179–185.

Wang, C., Ling, Z., and Pipeleers, D. (2005). Comparison of cellular and medium insulin and GABA content as markers for living beta-cells. Am. J. Physiol. Endocrinol. Metab. *288*, E307–E313.

Wilmanski, T., Zhou, X., Zheng, W., Shinde, A., Donkin, S.S., Wendt, M., Burgess, J.R., and Teegarden, D. (2017). Inhibition of pyruvate carboxylase by 1α,25-dihydroxyvitamin D promotes oxidative stress in early breast cancer progression. Cancer Lett. *411*, 171–181.

Xia, J., and Wishart, D.S. (2011). Web-based inference of biological patterns, functions and pathways from metabolomic data using MetaboAnalyst. Nat. Protoc. *6*, 743–760.

Xu, J., Han, J., Long, Y.S., Epstein, P.N., and Liu, Y.Q. (2008). The role of pyruvate carboxylase in insulin secretion and proliferation in rat pancreatic beta cells. Diabetologia *51*, 2022–2030.

Yang, M., and Vousden, K.H. (2016). Serine and one-carbon metabolism in cancer. Nat. Rev. Cancer *16*, 650–662.

STAR★METHODS

KEY RESOURCES TABLE

REAGENT or RESOURCE	SOURCE	IDENTIFIER
Antibodies		
GCLC polyclonal rabbit antibody	Bio-Rad Laboratories	Cat# VPA00695
β-Actin monoclonal mouse antibody	Millipore Sigma	Cat# A2228; RRID: AB_476697
PCB monoclonal mouse antibody	Santa Cruz	Cat# sc-271493; RRID: AB_10649369
Bacterial and virus strains		
One Shot STABL3 cells	Sigma Aldrich	C737303
Chemicals, peptides, and recombinant proteins		
BAD $SAHB_A$ SD peptide human: NLWAAQRYGRELRXBDDXFVDSFKK	Fu et al., 2020	N/A
BAD $SAHB_A$ AAA peptide human: NLWAAQRYGREARXBAAXFVDSFKK	Fu et al., 2020	N/A
BAD $SAHB_A$ SD peptide mouse: WAAQRYGRELRXBDDXFEGSFK	Danial et al., 2008	N/A
BAD $SAHB_A$ AAA peptide mouse: WAAQRYGREARXBAAXFEGSFK	Danial et al., 2008	N/A
Human IL-1β	R&D Systems	201LB/CF
Human TNFα	R&D Systems	210TA/CF
Human IFNγ	R&D Systems	285IF/CF
Mouse IL-1β	R&D Systems	401-ML/CF
Mouse TNFα	R&D Systems	410-MT/CF
Mouse IFNγ	R&D Systems	485-MI/CF
GEA3162	Enzo Life Sciences	CAS: 144575-47-3: ALX-430-004
CM-H2DCFDA	Thermo Fisher Scientific	C6827
L-buthionine sulfoximine (BSO)	Tocris Biotechne	CAS: 83730-53-4, 6954
N-acetyl-cysteine (NAC)	Sigma-Aldrich	CAS: 616-91-1, A9165
Accustase	EMD Millipore Sigma	SCR005
Prodo Islet Media (Standard)	Prodo Labs	PIM(S)
Human A/B serum	Gemini	100-512
RPMI 1640 media	GIBCO	11875135
Fetal Bovine Serum	Gemini	100-106
Tert-butyl hydroperoxide 70% solution	Sigma-Aldrich	B2633
Methanol, Optima LC/MS grade	Fisher Chemical	A456-212
Water, Optima LC/MS grade	Fisher Chemical	W6500
Hexakis(1H, 1H, 3H-Tetrafluoropropoxy) Phosphazene	Agilent Technologies	CAS: 58943-98-9
Glucose-$^{13}C_6$	Cambridge Isotope Laboratories	CAS: 110187-42-3
Inosine-$^{15}N_4$	Cambridge Isotope Laboratories	CAS: 58-63-9:
Thymine-d_4	Cambridge Isotope Laboratories	CAS: 200496-79-3:
Glycocholate-d_4	Cambridge Isotope Laboratories	CAS: 1201918-15-1
Luna-HILIC column	Phenomenex	00D-4449-E0
Scherzo SM-C18 column 3 μm, 3.0 × 150 mm with guard	Imtakt Corp	SM035

(*Continued on next page*)

Continued

REAGENT or RESOURCE	SOURCE	IDENTIFIER
Critical commercial assays		
AnnexinV/7AAD Staining kit	BD Biosciences	BDB559763
CM-DCFDA Staining kit	Invitrogen	C6827
Glutathione Colorimetric Assay kit	BioVision Inc.	K26-100
Deposited data		
Non-targeted metabolomics data with annotations	This paper; Fu et al., 2020	ST001953
Experimental models: Cell lines		
293T human cell line	Sigma Aldrich	12022001
Insulinoma-1 rat beta cell line (INS-1 832/13)	Gift from Dr. Richard Kibbey, and are available from MilliporeSigma	SCC208
Experimental models: Organisms/strains		
C57BL/6J mice	The Jackson Laboratory	000664
Recombinant DNA		
Human PC in pDNR223	Harvard Plasmid Database	HsCD00375392
pLenti7.3 vector	Invitrogen	V53406
Human PC shRNA lentivirus	Fu et al., 2020	N/A
Mouse PC shRNA lentivirus	Fu et al., 2020	N/A
pCDH BAD SD	Fu et al., 2020	N/A
pCDH BAD AAA	Fu et al., 2020	N/A
pCDH vector	Addgene	72265
Mito-Orp-1-roGFP2 AV (Invitrogen, pAdeno CMV backbone)	Gutscher et al., 2009, Shum et al., 2021	N/A
Cyto-Orp-1-roGFP2 AV (Invitrogen, pAdeno CMV backbone)	Gutscher et al., 2009, Shum et al., 2021	N/A
Mito-Grx1-roGFP2 AV (Invitrogen, pAdeno CMV backbone)	Gutscher et al., 2008, Shum et al., 2021	N/A
Cyto-Grx1-roGFP2 AV (Invitrogen, pAdeno CMV backbone)	Gutscher et al., 2008, Shum et al., 2021	N/A
Software and algorithms		
MassHunter Quantitative Analysis Software	Agilent Technologies	N/A
Metaboanalyst V4.0	Pang et al., 2020	N/A
Prism 9 for MacOS (Version 9.0.0)	GraphPad Software, LLC	N/A
FACSDiva Analytical software	BD Biosciences	N/A

RESOURCE AVAILABILITY

Lead contact

Further information and requests for resources and reagents should be directed to and will be fulfilled by the Lead Contact, Nika N. Danial (nika_danial@dfci.harvard.edu).

Materials availability

This study did not generate any unique reagents. The corresponding author can be contacted for further details.

Data and code availability

- The metabolomics data in Figures 1 and S1 were analyzed from a dataset that is publicly available and deposited in NIH Common Fund's National Metabolomics Data Repository (NMDR), https://www.metabolomicsworkbench.org, and the study has the DOI https://dx.doi.org/10.21228/M8F121. The accession number is listed in the key resources table.
- This study did not generate or report original code.
- Any additional information required to reanalyze the data reported in this paper is available from the lead contact upon request.

EXPERIMENTAL MODEL AND SUBJECT DETAILS

Human islets

Primary cadaveric human islets were isolated by the Alberta Islet Distribution Program (University of Alberta) and by the Integrated Islet Distribution Program (IIDP) at City of Hope (https://iidp.coh.org/). All donor material was obtained with informed consent and de-identified patient information, qualifying all human islet distribution centers as IRB-exempt and thus exempt from requiring approval by the office for human research studies at Dana-Farber Cancer Institute. A total of 62 human donors were used in this investigation with mean age of 42.9 ranging from 17-60 years of age, 74% and 26% of which were males and females, respectively. The average BMI of donors was 26.4 (range 19.6-34.4), and baseline islet viability was 92.1% (range 77%–99%). Additional information on the islet donor material used per experiment can be found in Table S3.

Mouse islets

Primary mouse islets were isolated from 12 week-old C57BL/6J male and C57BL/6N (Charles River Laboratories) male and female wild-type mice and cultured and maintained in RPMI media (GIBCO) as previously described (Ljubicic et al., 2015; Fu et al., 2020).

METHOD DETAILS

Islet culture, cytokine and NO donor treatment

Human islets were maintained in PIM(S) media (Prodo Labs) with 5% human A/B serum (Gemini BioProducts) at a density of 1000 islets per 10 mL as previously described (Fu et al., 2020). Unless otherwise stated, human and mouse islets were cultured in 5.8 and 11 mM glucose, respectively. The cocktail of inflammatory cytokines (R&D Systems) used to treat human islets consisted of 10 ng/ml TNF-α, 10 ng/ml IL-1β, and 100 ng/ml IFNγ, and that used to treat mouse islets consisted of 20 ng/ml TNF-α, 40 ng/ml IL-1β, and 10 ng/ml IFNγ, with PBS serving as control for cytokine treatment (Fu et al., 2020; Ljubicic et al., 2015). Islets were treated with vehicle control DMSO (0.5%) or NO donor (GEA3162) at 40 μM. This concentration was chosen based on pilot dose response analyses (data not shown), indicating that it caused the highest increase in NO levels in human islets and is within commonly used dose range (Ljubicic et al., 2015; Taylor et al., 2004; Wang et al., 2005). For BSO, we tested a pharmacologically relevant dose range (10-250 μM) and identified a concentration that sufficiently reduced GSH levels. Human islets and mouse islets were treated with 250 μM BSO and 1 mM NAC or an equal volume of H_2O (vehicle for BSO or NAC). All pharmacologic treatments occurred alongside cytokine or NO donor treatment, 24 or 48 h prior to ROS and viability measurements, respectively.

SAHB synthesis and treatment

Peptide synthesis were performed as previously described (Danial et al., 2008; Ljubicic et al., 2015). SAHBs corresponding to human and mouse BAD BH3 domain variants were used for treatment of human and mouse islets, respectively. $SAHB_A$ SD is modeled after phospho-mimic S118 and S155 in the human and mouse BAD sequence, respectively (Danial et al., 2008; Ljubicic et al., 2015; Szlyk et al., 2014). $SAHB_A$ AAA is modeled after a triple Ala mutant in the BAD BH3 domain that modifies L151, S155 and D156 in the mouse BH3 domain and their corresponding residues in the human BAD BH3 sequence (Giménez-Cassina et al., 2014; Ljubicic et al., 2015). For human islet, mouse islet and INS-1 cell treatments in ROS, survival and metabolomics assays, cells were treated for 5 h with 5 μM of the indicated SAHBs in 0.5% DMSO in uptake medium, which consisted of RPMI for mouse islets and INS-1 cells or PIM(S) for human islets at pH 6.2, which is the optimal pH for cellular uptake of BAD stapled peptides. Control islets were treated with vehicle composed of 0.5% DMSO in uptake medium. Islets were then washed and left to recover in complete physiological medium (pH 7.4) prior to any further treatments or assays.

Untargeted metabolomics

Human islets from 5 independent donors were treated as indicated, rinsed in 150 mM ammonium formate and stored at −80°C. 150 human islets per replicate were extracted in hot 70% ethanol at 75°C for 3 min, placed on ice, and clarified by centrifugation. Extracts from all donors were pooled and analyzed in 8 replicates by flow-injection, non-targeted metabolomics in negative ionization mode on an Agilent 6550 Quadrupole Time-of-flight mass spectrometer (Agilent Technologies) as previously described (Fuhrer et al., 2011). These analyses were performed using the services provided by General Metabolics, LLC. For sample extracts, 1.5 μl was injected using a MPS3 autosampler (Gerstel). The mobile phase contained isopropanol/water (60:40, v/v) 1 mM ammonium fluoride with a flow rate of 150 μl per min. Mass spectra were recorded in profile mode from m/z 50 to 1000 with a frequency of 1.4 spectra/s for 0.48 min using maximum resolving power (4 GHz HiRes). For online mass axis correction, homotaurine and hexakis (1H, 1H, 3H tetrafluoropropoxy) phosphazine (HP-0921, Agilent Technologies) were spiked in the mobile phase. Source temperature was 325°C, with 5 L per min drying gas and a nebulizer pressure of 30 psig. Ions were putatively annotated by matching their measured mass with compounds in the KEGG database for *Homo sapiens*, allowing a tolerance of 0.001 Da, only deprotonated ions (without adducts) were included and duplicate matches were retained. Data are presented as relative to vehicle PBS control showing the cytokine-treated samples (Figures 1 and 3A).

Targeted metabolomics by LC-MS/MS

Multiple orthogonal platforms (Methods A, B, C and D, detailed below) were used based on the chemical nature of metabolites of interest (see also Table S2). For glutathione, methods A, C and D were used to rigorously cross-validate the observed trends. For steady state levels of SAM, cystathionine, GSH and GSSG in Figure 1 and that of cysteine and cystine in Figure 3A, Method A was used. For GSH/GSSG in Figure 6G, glutathione and other sulfhydryls were protected from oxidation reactions by washing and extracting in the presence of 1 mg/ml NEM (N-ethylmaleimide) and analyzed using Method C (Russo et al., 2020). Glycolytic intermediates in INS-1 cells (Figure S1B) were also quantified using Method B. Briefly, islets from individual donors with 300 islets per replicate, or 5×10^6 million INS-1 cells per replicate, were washed with 150 mM ice-cold ammonium formate pH 7.4 containing 1mg/ml NEM. Cells were scraped into 380 μl of 50% methanol (1mg/ml NEM) and placed into Eppendorf tubes. A volume of 220 μL of acetonitrile was added to each sample. Cells were lysed by sonication and 600 μl of dichloromethane and 300 μl of water were added to samples followed by vortex mixing. Samples were allowed to phase separate on ice for 10 min. They were then centrifuted for 10 min at 1500xg (4000 rpm). The upper layer was transfered to a fresh pre-chilled tube and dried by vacuum centrifugation at 4°C. Samples were resuspended in 30 mL of Optima LC/MS grade H_2O for 5 μL injections analyzed by Method A and Method B.

Method A details: Extracts as prepared above were analyzed by UPLC/QQQ (Agilent 6430 triple quadrupole mass spectrometer, Agilent Technologies). Chromatographic separation was achieved using a Scherzo SM-C18 column 3 μm, 3.0 × 150 mm with guard (Imtakt Corp). The chromatographic gradient started at 100% mobile phase A (0.2% formic acid in water) with a 2 min hold followed by a 6 min gradient to 80% B (0.2% formic acid in MeOH) at a flow rate of 0.4 mL per min. The column was washed at 100% mobile phase B for 5 min and re-equilibrated for 6 min at 100% mobile phase A before next injection. Eluant ionization was achieved using positive electrospray ionization (ESI). Ion source gas temperature and flow were set at 350°C and 10 l/min respectively, nebulizer pressure was set at 40 psi and capillary voltage was set at 3500V.

Method B details: Extracts as prepared above were analyzed by UPLC/QQQ (Agilent 6470 triple quadrupole mass spectrometer, Agilent Technologies) with 5 μl injections. Chromatographic separation was achieved using a Intrada-AA column 3 μm, 3.0 × 150 mm with a unison guard (Imtakt Corp). The chromatographic gradient started at 100% mobile phase B (0.3% formic acid in acetonitrile) with a 3 min gradient to 27% mobile phase A (100 mM ammonium formate in 20% acetonitrile) followed by an 18.5 min gradient to 100% mobile phase A at a flow rate of 0.6 mL per min. The column was washed at 100% mobile phase A for 5.5 min then returned to 100% B over one min and re-equilibrated for 7 min at 100% mobile phase B before next injection.

Method C details: Extracts as prepared above were analyzed by UPLC/QQQ (Agilent 6430 triple quadrupole mass spectrometer, Agilent Technologies). Chromatographic separation was achieved using a Scherzo SM-C18 column 3 μm, 3.0 × 150mm (Imtakt Corp, JAPAN) maintained at 10°C. The chromatographic gradient started after a 2 min hold at 100% mobile phase A (100 mM formic acid in water) with a 6 min gradient to 80% B (200 mM ammonium formate in 30% ACN, pH 8) at a flow rate of 0.4 ml/min. The gradient was followed by a 5 min hold time at 100% mobile phase B and a subsequent re-equilibration time (6 min) before next injection. Compounds were ionized by ESI in negative ionization mode.

For methods **A-C**, an external calibration curve was generated by serial dilution of standards dissolved in water. Sample area under the curve was compared to the external calibration curve using Mass Hunter Quant (Agilent Technologies). No additional corrections for potential ion suppression effects were made, thus the quantitation is considered semiquantitative. Multiple reaction monitoring (MRM) transitions were optimized on authentic standards. Specific MRM transitions for metabolites detected by targeted methods in this study are shown in Table S2. Data are presented as fold change in concentrations for each individual donor, normalized to the median across 68 other metabolites detected, and shown relative to vehicle PBS set at 1. Details on statistical analysis are provided below under Metabolomics data analysis.

Method D details: This method was used for stable isotopic labeling analysis (SITA) of [$^{13}C_6$]-glucose incorporation into GSH. Human donor islets were label led for 24 h in RPMI media containing 5.8 mM [$^{13}C_6$]-glucose at a density of 100 islets/ml media. Islet were extracted by sonication in 80% methanol containing internal standards; inosine-$^{15}N_4$, thymine-d_4 and glycocholate-d_4 (Cambridge Isotope Laboratories). Extracts were centrifuged at 16,000 RPM 4°C for 20 min, supernatants were collected and loaded onto a Luna-HILIC column through an UltiMate-3000 TPLRS LC, with a mobile phase A (20 mM ammonium acetate and 20 mM ammonium hydroxide dissolved in 5:95 v/v acetonitrile/water) and 90% mobile phase B (10 mM ammonium hydroxide in 75:25 v/v acetonitrile/methanol). Metabolites were separated with a 10 min linear gradient up to 99% mobile phase A. Mass analysis was carried out using a Q-Exactive HF-X mass spectrometer (Thermo Fisher Scientific). Negative modes were used with full scan analysis over m/z 70-750 m/z at 60,000 resolution, 1e6 AGC, and 100 ms maximum ion accumulation time. Additional settings were: ion spray voltage of 3.8 kV; capillary temperature of 350°C; probe heater temperature of 320°C; sheath gas of 50; auxiliary gas of 15; and S-lens RF at level 40.

Detection of GSH/GSSG by colorimetric assay

This method was used to provide additional/independent confirmation of changes in GSH and GSSG levels obtained by mass spectrometry methods, and are presented in Figure 6A. Briefly, human and mouse islets sampled at 100 islets per replicate were collected and stored at −80°C prior to extraction. Measurement of GSH and GSSG was done using colorimetric reaction-based detection

method (BioVision). Briefly, GSH in extracts was reacted with Ellman's reagent (DTNB) to produce 2-nitro-5-thiobenzoic acid and a yellowish color, which is detected at 412 nM in the plate reader. GSSG in the extracts was then reduced back to GSH in another step and made to further react with Ellman's reagent and produce increasing yellowish color detected at 412 nM, allowing for extrapolation of GSSG levels from total cellular GSH.

Genetic manipulation of islets

Lentiviruses for shRNA targeting of *PC*, PC overexpression or full length BAD S155D and AAA variants were generated according to the MISSION lentiviral packaging protocol (Sigma). Islets were transduced using 150 μl of viral supernatants per 100 islets. For viability assays, islets were transduced and 24 h later were treated with cytokine or NO donor for 48 h. For ROS measurements and metabolomics studies, islets were transduced and 48 h later were treated with cytokine or NO donor for 24 h. As such, all assays involved a total of 72 h of knockdown or overexpression.

Quantification of ROS and cell survival by flow cytometry

ROS levels were measured 24 h after cytokine or NO donor treatment. Briefly, 50 islets per replicate were gently dispersed in accutase (Millipore Sigma) at 37°C, rinsed in 1 mL PBS, and stained at 37°C for 30 min with CM-H2DCFDA or at room temperature for 15 min with AnnexinV/7AAD. Cells were monitored for PE/APC (585 nm/660nm) or FITC/DCF (530 nm/488 nm) fluorescence using a BD FACSCanto II flow cytometer (BD Biosciences) and FACSDiva software (BD Biosciences). Positive cells were identified by comparison to unstained cells for all wavelengths at least 2 s.d. outside the means of unstained samples. ROS levels were calculated as %DCFDA fluorescence by normalizing the total DCFDA signal intensity to an internal control of maximal DCFDA signal for each sample set to 100%. The internal control was obtained by treating cells with tert-butyl hydroperoxide (100 μM) for 5 min to remove discrepancies in dye uptake between samples and independent experiments. Cell survival/death was quantified 48 h after cytokine or NO donor treatment by staining islets with AnnexinV/7AAD (BD Biosciences) as previously described (Fu et al., 2020; Ljubicic et al., 2015).

Islet re-aggregation, biosensor expression and quantification of Grx1- and Orp1-roGFP2 fluorescence

Grx1 and Orp1 biosensors were expressed, analyzed and imaged in islets as previously described (Shum et al., 2021). Human islets were dissociated with accutase (500 μl per 200 islets) at 37°C for 10 min followed by manual pipetting. Islets were then rinsed twice in media, pelleted, resuspended in media and counted. Dissociated islets were seeded into 96 well v-bottom plates (Nunc) at $2.5x10^3$ cells per well, re-aggregated by centrifugation at 1200 RPM for 5 min and exposed to adenoviruses expressing cytosolic or mitochondrial Grx1-roGFP2 or Orp1-roGFP2 at an MOI of 100 for 2 h. The adenoviruses were washed out with 3 equal volume media rinses with centrifugation. Islets were re-aggregated by centrifugation at 1200 RPM for 5 min and cultured for 48 h before imaging. Islet re-aggregates were treated with vehicle or BAD $SAHB_A$ SD in the presence of PBS or cytokines for 24 h prior to imaging. Live imaging with temperature (37°C) and atmospheric (CO_2 5%) control was performed on a Nikon Eclipse Ti microscope with a Nikon Plan Fluor ELWD 20X/0.45 Ph1 DM/ infinity/0-2 WD 7.4 objective and images were captured with a Nikon T-P2 camera (Nikon Instruments Inc.). This low magnification allowed the entire re-aggregated islet to be imaged within the field of view and maximized data sampling. Image acquisition was performed using NIS-Elements AR analysis 4.30.02 (Nikon Instruments Inc.), and image analysis was performed using Fiji ImageJ (Version: 2.0.0-rc-59/1.51n, Build: fab6e1a004) for ratiometric intensity (405 nm/488 nm) quantitation of regions of interest using the image calculator process to divide images at 405 nm by the corresponding images at 488 nm. This generated a new ratiometric image from the raw image data, and the lookup table 'fire' arbitrary color intensity scale was assigned onto the ratiometric images.

QUANTIFICATION AND STATISTICAL ANALYSIS

Data are presented as mean ± SEM of the indicated number of human islet donors or independent experiments in the figure legends. Statistical significance was determined by one or two-way ANOVA with Tukey's test for multiple means comparisons and Student's t test were used in GraphPad for calculating statistical significance with q-value adjustments for a false discovery rate (FDR) of 1%. No outliers were removed as all data were determined inclusive using two-sided Grubbs with alpha set to 0.05.

Metabolomics data and statistical analysis

All data except the untargeted metabolomics analysis were quantified by integrating the area under the curve of each metabolite using MassHunter Quant (Agilent Technologies). Pathway enrichment analyses were performed using Metaboanalyst software (https://www.metaboanalyst.ca/) based on KEGG metabolic pathways. Pathway analysis was performed comparing the relative metabolite levels between BAD $SAHB_A$ SD and vehicle, in the presence of cytokines (Figure S1A). The impact score represents the number of nodes contained in the data and the adjusted p value was obtained using Holm adjustments (Xia and Wishart, 2011). Targeted processing of GSH and isotopolog for data collected using LCMS "method D" was conducted using TraceFinder software version 4.1 (Thermo Fisher Scientific). Compound identities were confirmed using reference standards. GSH metabolite isotopolog abundances were normalized to the recovery of internal standards inosine-$^{15}N_4$, thymine-D_4 and glycocholate-D_4. Total ion counts of each mass isotopolog of GSH were corrected for natural abundances of ^{13}C and fractional labeling out of the total pools of GSH were calculated in Excel.

Cell Reports, Volume *37*

Supplemental information

Glucose metabolism and pyruvate carboxylase enhance glutathione synthesis and restrict oxidative stress in pancreatic islets

Accalia Fu, Lara van Rooyen, Lindsay Evans, Nina Armstrong, Daina Avizonis, Tatsuya Kin, Gregory H. Bird, Anita Reddy, Edward T. Chouchani, Marc Liesa-Roig, Loren D. Walensky, A.M. James Shapiro, and Nika N. Danial

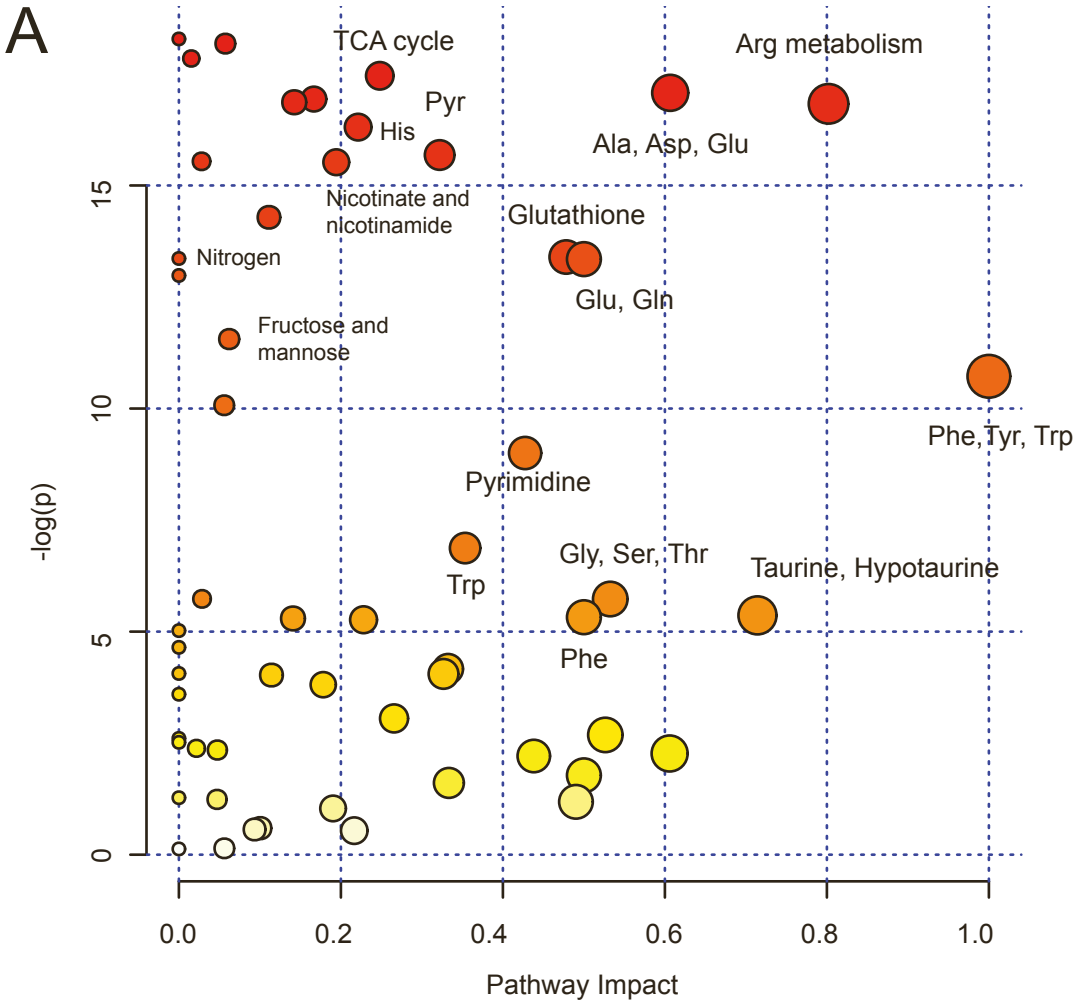

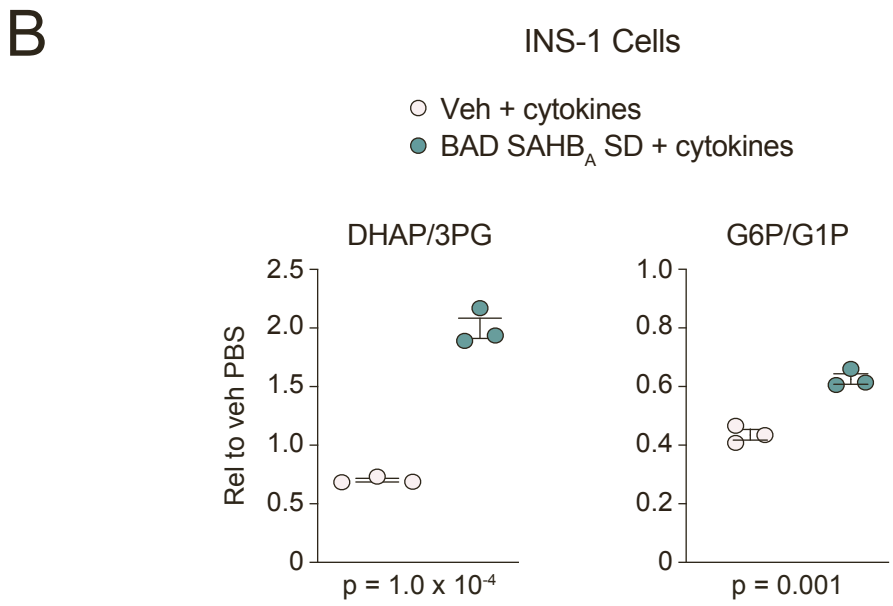

Fu et al, Figure S1

Figure S1, related to Figure 1. Pathway analysis of untargeted metabolomics data obtained from human islets protected with phospho-BAD mimicry during inflammation stress.

(A) Metabolome view depicting Holm-adjusted -log p-value (y-axis) of matched pathways from pathway enrichment analysis based on the KEGG metabolic pathways database comparing BAD $SAHB_A$ SD- vs vehicle-treated human islets. Pathway impact score calculated from topology analyses and number of entities (metabolites) is represented on the x-axis to reveal the most statistically significant changes that have the highest impact on a given pathway (top right on plot). The node color is based on its p-value and the node radius is determined based on pathway impact values.
(B) LC-MS/MS based quantification of DHAP/3-phosphoglycerate and glucose-6-phosphate/glucose-1-phosphate in INS-1 cells treated with vehicle or BAD $SAHB_A$ SD and exposed to cytokines (n=3).

Data in (B) are represented as means ± SEM. Statistical analyses are student's t-test.

See also Tables S1 and S2.

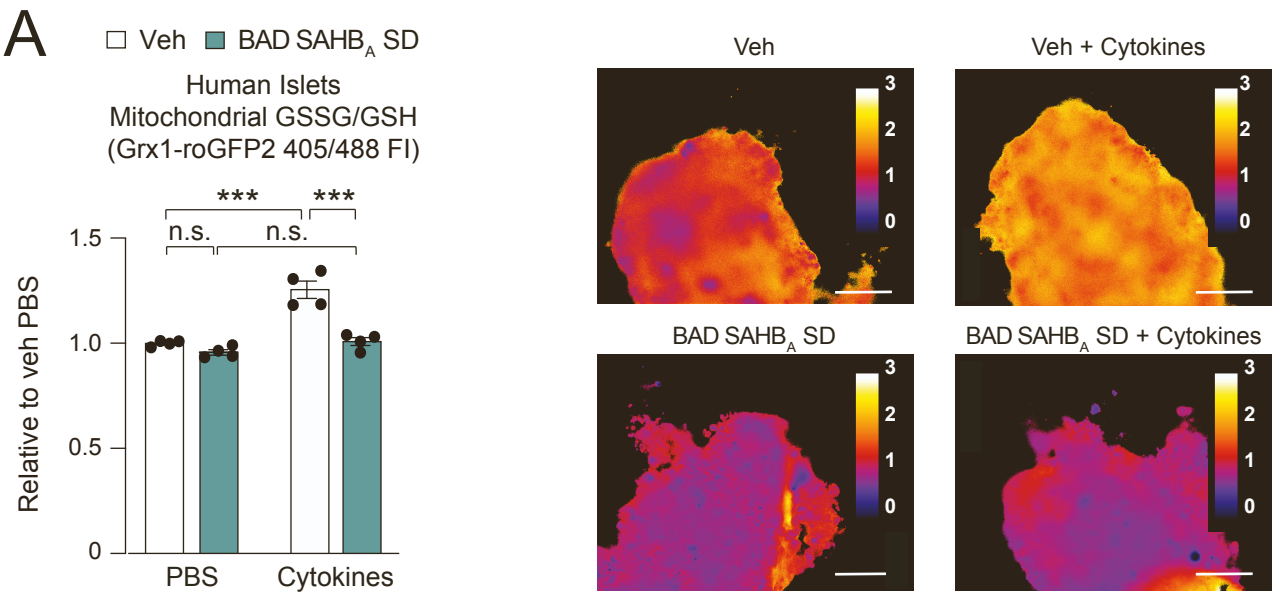

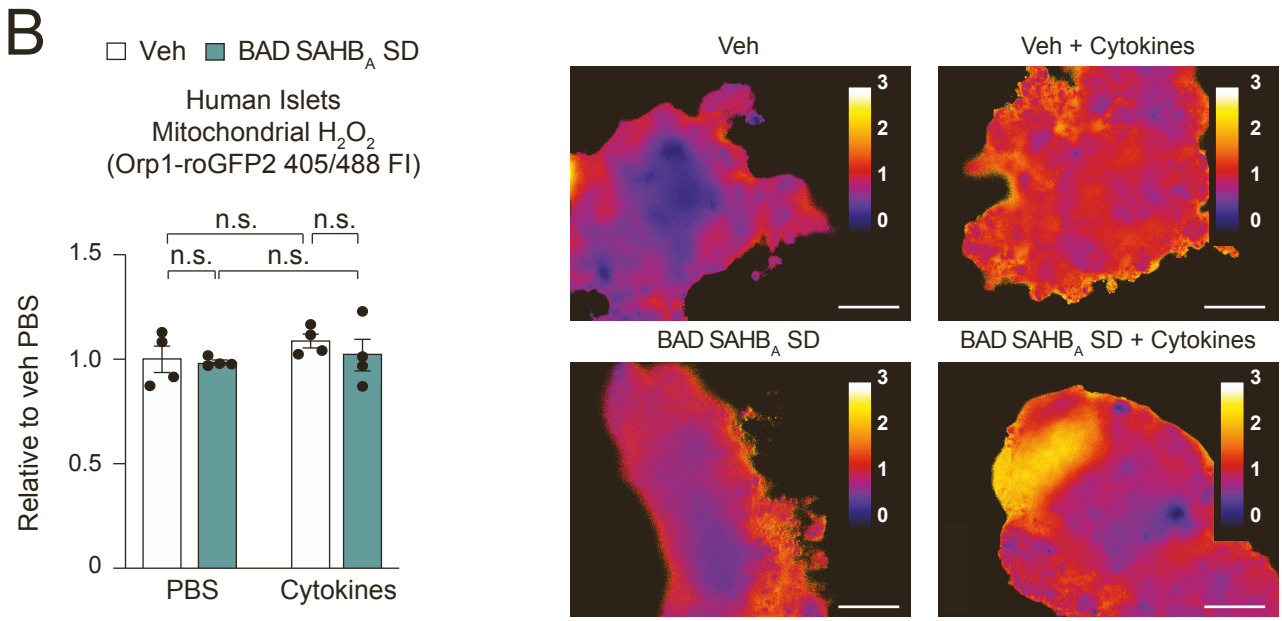

Fu et al, Figure S2

Figure S2, related to Figure 3. The effect of phospho-BAD mimicry on redox coupling in human islets undergoing inflammation stress.

(A) Quantification (left) and representative images (right) of ratiometric fluorescence intensity in re-aggregated human islets expressing mitochondrial Grx1-roGFP2 that were treated with veh or BAD $SAHB_A$ SD in the presence of PBS or cytokines for 24 h (n=4). Scale bars, 100 microns.

(B) Quantification (left) and representative images (right) of ratiometric fluorescence intensity in re-aggregated human islets expressing mitochondrial Orp1-roGFP2 that were treated with veh or BAD $SAHB_A$ SD in the presence of PBS or cytokines for 24 h (n=4).

Data are represented as means ± SEM. ***$p < 0.0005$; n.s., non-significant; two-way ANOVA withTukey's adjustment for multiple comparisons.

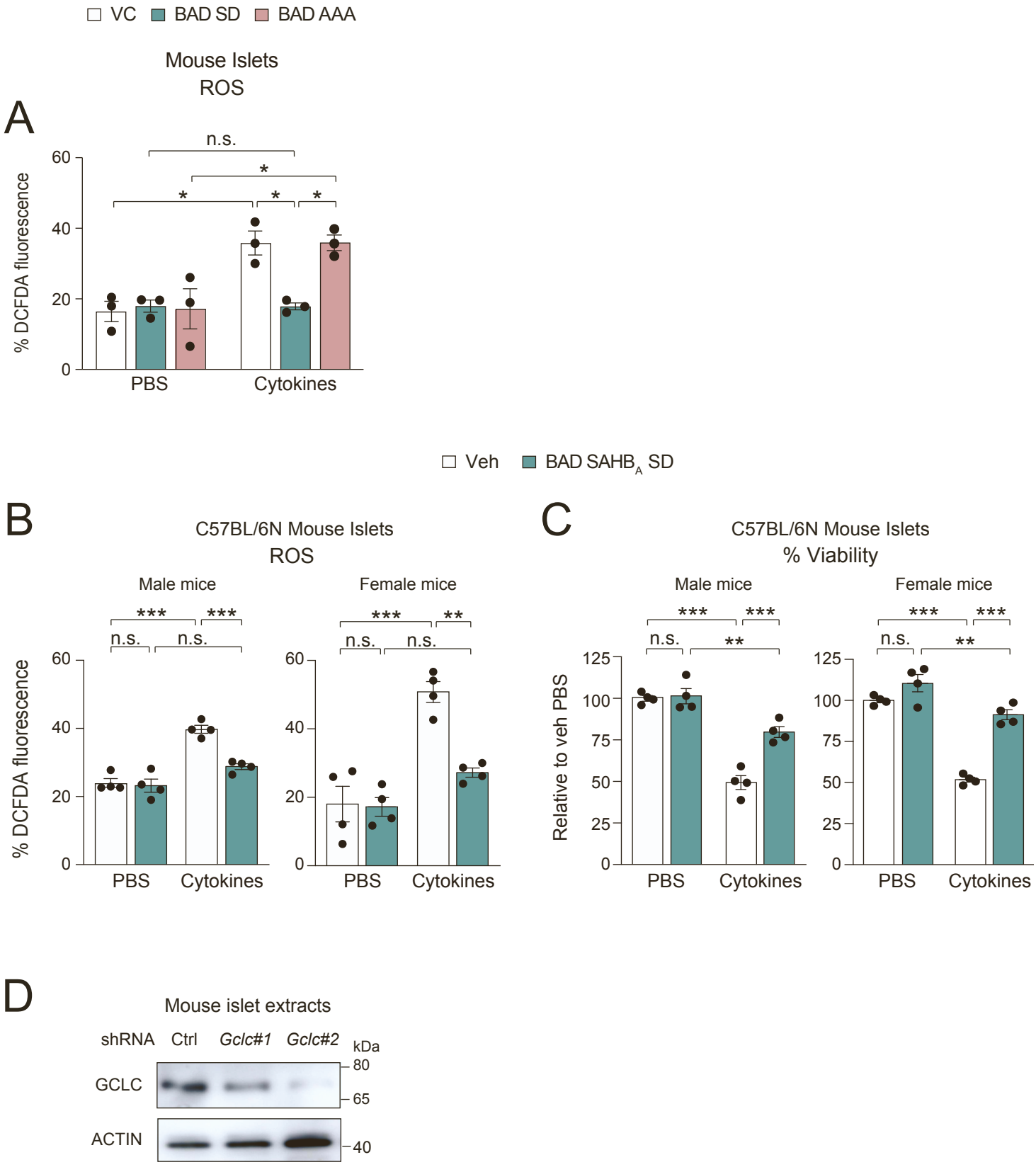

Fu et al, Figure S3

Figure S3, related to Figure 4. The effect of phospho-BAD mimicry on ROS levels.

(A) ROS levels in vector control-, BAD SD-, and BAD AAA-expressing mouse islets exposed to cytokines for 24 h (n=3).
(B-C) ROS levels (B) and viability (C) of mouse islets isolated from male and female C57BL/6N mice and treated with vehicle or BAD $SAHB_A$ SD and cultured in the presence of PBS or cytokines for 24 h (B) or 48 h (C) (n=4).
(D) Western blot analysis of *GCLC* knockdown efficiency using two independent hairpins compared with control (Ctrl) shRNA for data shown in Figures 4E and F.

Data are represented as means ± SEM. *$p < 0.05$, **$p < 0.005$, ***$p < 0.0005$; n.s., non-significant; two-way ANOVA with Tukey's adjustment for multiple comparisons.

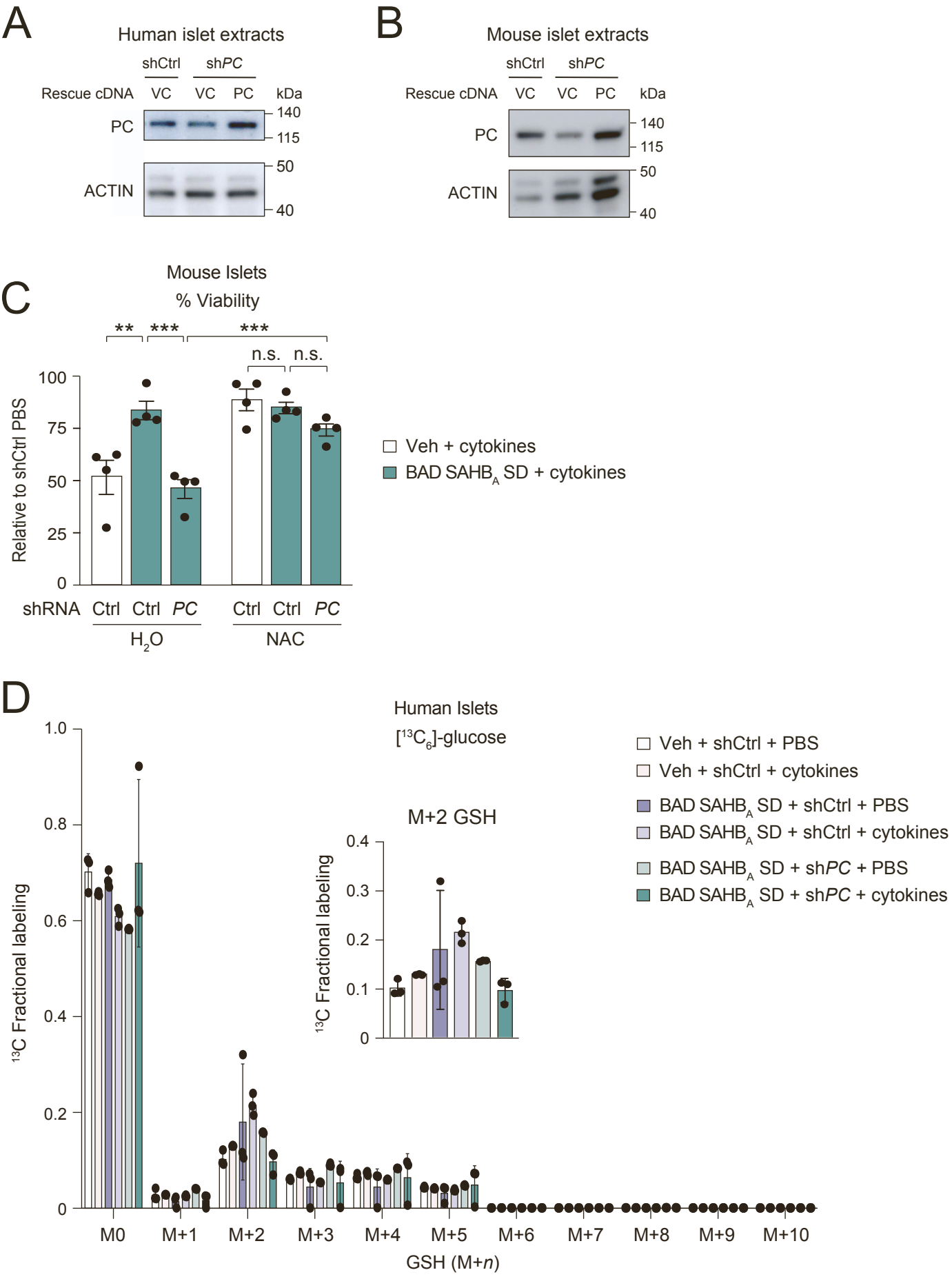

Fu et al, Figure S4

Figure S4, related to Figure 5. PC mediates the antioxidant effect of phospho-BAD mimicry.

(A-B) Western blot analysis of *PC* knockdown and rescue in human (A) and mouse (B) islets for experiments shown in Figures 5A and B.
(C) Viability of mouse islets transduced with lentiviruses bearing control (Ctrl) or *PC* shRNA and treated as in Figure 5C, measured 48 h following cytokine treatment.
(D) Non-normalized total fractional labeling for each mass isotopolog of GSH (M+*n*), including unlabeled GSH (M+0), in the experiment shown in Figures 5D and E.

Data are represented as means ± SEM. **p < 0.005, ***p < 0.0005; n.s., non-significant; two-way ANOVA with Tukey's adjustment for multiple comparisons.

Mass spectrometry platforms

Untargeted metabolomics

	Ion signal intensity				p-value			
	Veh PBS	BAD $SAHB_A$ SD PBS	Veh cytokines	BAD $SAHB_A$ SD cytokines	Veh PBS vs SD PBS	Veh PBS vs Veh cytokines	SD PBS vs SD cytokines	Veh cytokines vs SD cytokines
Cysteinylglycine	0.939	0.999	0.886	1.046	0.541	0.643	0.715	6.42E-03
Glutamate	79.61	85.49	63.21	81.67	0.215	3.50E-05	0.576	5.41E-06
Glycine	1.905	1.776	2.992	2.372	0.494	8.79E-12	2.24E-06	1.13E-06
GSH	46.63	53.56	33.41	45.72	0.012	4.22E-06	0.004	1.34E-05
GSSG	0.371	0.444	0.395	0.455	0.003	0.554	0.932	0.017
Hypotaurine	0.243	0.307	0.108	0.195	0.037	8.90E-06	1.55E-04	0.003
Methionine	1.149	1.168	1.975	1.989	0.982	<1E-15	<1E-15	0.992
Oxoproline	215.9	229.3	381.6	326.6	0.423	<1E-15	3.95E-11	3.99E-06
Phosphoserine	2.24	2.598	1.568	2.53	0.006	1.34E-06	0.904	1.07E-09
Serine	2.062	1.359	10.04	5.002	1.86E-04	<1E-15	<1E-15	<1E-15
Taurine	62.06	64.71	48.42	61.33	0.54	8.09E-07	0.329	2.16E-06

Targeted metabolomics

	Concentration (μM)				p-value			
	Veh PBS	BAD $SAHB_A$ SD PBS	Veh cytokines	BAD $SAHB_A$ SD cytokines	Veh PBS vs SD PBS	Veh PBS vs Veh cytokines	SD PBS vs SD cytokines	Veh cytokines vs SD cytokines
Cystathionine	291.1	279.7	554.8	665.3	0.97	2.73E-06	1.25E-08	0.017
GSH	1.843	2.465	6.239	10.49	0.972	0.035	2.34E-04	0.043
GSSG	2.768	4.054	13.52	14.27	0.806	5.60E-06	2.47E-05	0.921
SAM	1.354	1.725	0.946	1.245	9.70E-04	3.84E-04	6.47E-05	0.006
γ-Glutamylcysteine	1.171	1.581	1.745	1.815	0.509	0.235	0.849	0.995
Cysteine	117.5	464.5	137.2	146.7	1.76E-05	0.979	5.02E-05	0.997

Table S1, related to Figures 1 and 3A. Levels of metabolites related to glutathione metabolism and statistical comparisons across all experimental conditions.

Metabolite	Quantifying transition	Qualifying transition	Method
S-adenosylmethionine	399→136	399→97	A
L-cystathionine	223→74	223→88	A
L-cysteine	122→76	122→59	A
L-cystine	259→97	259→79	A
DHAP/3PG	187→141	187→99 and 81	B
G6P/G1P	241→120	241→74	B
Reduced glutathione	308→179	308→76	C
Oxidized glutathione	613→355	613→231	A and C
NEM-glutathione	433.1→59	433.1→201	C

Table S2, related to Figures 1 and S1B. MRM (multiple reaction monitoring) and SRM (specific reaction monitoring) transitions for metabolites quantified by UPLC/ and HPLC/QQQ.

Figure	Experiment	Donor #	Source	Sex	Age	BMI	Viability %
1, S1	Targeted metabolomics (Cystathione, glu-cys, GSH, GSSG, SAM)	13	UA	M	42	33.3	77
		14	UA	M	54	28.7	88.5
		15	UA	M	48	30.2	88
		RRID:SAMN08769822	IIDP	M	20	24.4	99
		RRID:SAMN08769393	IIDP	F	53	31.9	95
	Untargeted metabolomics	RRID:SAMN08769822	IIDP	M	20	24.4	99
		RRID:SAMN08769393	IIDP	F	53	31.9	95
		RRID:SAMN08769195	IIDP	M	17	25.6	94
		RRID:SAMN08769080	IIDP	M	49	26.3	95
		RRID:SAMN08769078	IIDP	M	45	24.6	90
2A-D, 5D-E	Targeted metabolomics Glucose tracer into GSH	99	UA	M	29	20.8	88.5
		100	UA	M	60	23.8	91
		RRID:SAMN19470079	IIDP	M	39	27.5	95
		RRID:SAMN19920583	IIDP	M	54	24.5	95
3A	Untargeted metabolomics (GSH, GSSG, pyruvate, malate)	RRID:SAMN08769822	IIDP	M	20	24.4	99
		RRID:SAMN08769393	IIDP	F	53	31.9	95
		RRID:SAMN08769195	IIDP	M	17	25.6	94
		RRID:SAMN08769080	IIDP	M	49	26.3	95
		RRID:SAMN08769078	IIDP	M	45	24.6	90
3A	Targeted metabolomics (cysteine/cystine)	13	UA	M	42	33.3	77
		14	UA	M	54	28.7	88.5
		15	UA	M	48	30.2	88
		RRID:SAMN08769822	IIDP	M	20	24.4	99
		RRID:SAMN08769393	IIDP	F	53	31.9	95
3B, S2	Grx1-roGFP2 sensor data	RRID:SAMN20209569	IIDP	F	45	21.9	97
3C, S2	Orp1-roGFP2 sensor data	RRID:SAMN20209569	IIDP	F	45	21.9	97
4A	ROS levels with BAD SD and AAA	98	UA	M	21	19.6	86.5
		99	UA	M	29	20.8	88.5
		100	UA	M	60	23.8	91
		RRID:SAMN19470079	IIDP	M	39	27.5	95
4C	ROS levels with -/+ BSO	RRID:SAMN18196260	IIDP	F	41	28	95
		98	UA	M	21	19.6	86.5
		99	UA	M	29	20.8	88.5
		100	UA	M	60	23.8	91
		RRID:SAMN19470079	IIDP	M	39	27.5	95
5A, 6E	ROS (sh*PC* cytokines and NO donor)	13	UA	M	42	33.3	77
		14	UA	M	54	28.7	88.5
		15	UA	M	48	30.2	88
		37	UA	F	57	34.3	96
5F	ROS (sh*PC* with NAC rescue)	99	UA	M	29	20.8	88.5
		100	UA	M	60	23.8	91
		101	UA	M	59	25.6	97.5
		RRID:SAMN19470079	IIDP	M	39	27.5	95
5G,	ROS (PC with cytokines)	16	UA	M	25	20.8	95.5

6F		17	UA	F	56	21.2	84.5
		RRID:SAMN08774796	IIDP	M	59	28.4	97
		RRID:SAMN08930666	IIDP	F	45	26.6	97
		86	UA	M	36	25	96.5
5H	PC Viability (-/+BSO)	RRID:SAMN08769195	IIDP	M	17	25.6	94
		86	UA	M	36	25	96.5
6F	Viability	37	UA	F	57	34.3	96
	(sh*PC* and NO donor)	RRID:SAMN08773856	IIDP	F	56	26.4	91
		RRID:SAMN08773865	IIDP	M	47	25.8	95
		RRID:SAMN08773762	IIDP	M	21	24.8	98
		RRID:SAMN08930666	IIDP	F	45	26.6	97
6G	Targeted metabolomics	87	UA	F	55	26	89.5
	GSH (NO donor)	88	UA	M	41	27.8	87.5
		89	UA	F	58	34.4	87
		90	UA	F	60	27.5	85
		91	UA	M	58	24.8	92.5

Table S3, related to Figures 1, 2A-D, 3A-C, 4A, 4C, 5A, 5D-H, 6E-G, S1A, S2, S4A and S4D. Additional metrics on human islet donors for this investigation separated per each experiment.